

Incorporating physical constraints in a deep probabilistic machine learning framework for coarse-graining dynamical systems

Sebastian Kaltenbach^a, Phaedon-Stelios Koutsourelakis^{a,*}

^a*Professorship of Continuum Mechanics, Technical University of Munich*

Abstract

Data-based discovery of effective, coarse-grained (CG) models of high-dimensional dynamical systems presents a unique challenge in computational physics and particularly in the context of multiscale problems. The present paper offers a data-based, probabilistic perspective that enables the quantification of predictive uncertainties. One of the outstanding problems has been the introduction of physical constraints in the probabilistic machine learning objectives. The primary utility of such constraints stems from the undisputed physical laws such as conservation of mass, energy etc that they represent. Furthermore and apart from leading to physically realistic predictions, they can significantly reduce the requisite amount of training data which for high-dimensional, multiscale systems are expensive to obtain (Small Data regime). We formulate the coarse-graining process by employing a probabilistic state-space model and account for the aforementioned equality constraints as virtual observables in the associated densities. We demonstrate how probabilistic inference tools can be employed to identify the coarse-grained variables in combination with deep neural nets and their evolution model without ever needing to define a fine-to-coarse (restriction) projection and without needing time-derivatives of state variables.

We advocate a sparse Bayesian learning perspective which avoids overfitting

*Corresponding author

Email addresses: `sebastian.kaltenbach@tum.de` (Sebastian Kaltenbach),
`p.s.koutsourelakis@tum.de` (Phaedon-Stelios Koutsourelakis)

and reveals the most salient features in the CG evolution law. The formulation adopted enables the quantification of a crucial, and often neglected, component in the CG process, i.e. the predictive uncertainty due to information loss. Furthermore, it is capable of reconstructing the evolution of the full, fine-scale system and therefore the observables of interest need not be selected a priori. We demonstrate the efficacy of the proposed framework by applying it to systems of interacting particles and an image series of a nonlinear pendulum. In both cases we identify the underlying coarse dynamics and can generate extrapolative predictions including the forming and propagation of a shock for the particle systems and a stable trajectory in the phase space for the pendulum.

Keywords: Bayesian machine learning, virtual observables, multiscale modeling, reduced order modeling, coarse graining

1. Introduction

High-dimensional, nonlinear dynamical systems are ubiquitous in applied physics and engineering. The computational resources needed for their solution can grow exponentially with the dimension of the state-space as well as with the smallest time-scale that needs to be resolved as this determines the discretization time-step. Hence the ability to construct reduced, *coarse-grained* descriptions and models that are nevertheless predictive of various observables and at time-scales much larger than then inherent ones, is an important task [1].

One strategy for learning such coarse-grained (CG) models is based on data generated by simulations of the fine-grained (FG) system. This can yield an automated solution especially in cases where domain knowledge is limited or absent. The derivation of CG models from data is also particularly relevant in domains where FG models are not available, such as in social sciences or biophysics [2], but data abound. Data-based methodologies have also been fueled by recent advances in statistical [3] or machine learning [4] which, in large part, have been enabled by large datasets (and the computational means to leverage them). We note nevertheless that coarse-graining tasks based on FG

simulation data exhibit some fundamental differences [5]. Firstly, the acquisition of FG simulation data is by-definition expensive and the reduction of the required FG simulations is one of objectives of CG model development. Secondly, in physical applications, significant information about the underlying physical/mathematical structure of the problem, and of the CG model in particular, is available. This information might come in the form of constraints that reflect e.g. undisputed physical principles such as conservation laws (e.g. mass, momentum, energy). Injecting this prior information into the CG models in combination with FG data in an automated fashion represents a significant challenge [6], particularly in the context of *probabilistic* models [7]. Such a capability would be instrumental not only in reducing the required amount of FG data, but more importantly, in enabling predictions under *extrapolative* settings as those arising e.g. when the initial conditions of the FG system are different from the ones contained in the data.

In this paper, we propose a generative, probabilistic (Bayesian) machine learning framework [8] which employs FG simulation data augmented by virtual observables to account for constraints. In contrast to most existing techniques which consider the problems of CG state variable discovery and CG model construction in two or more steps [9, 10, 11, 12], we address both simultaneously [13]. The framework proposed consists of two parts: a probabilistic coarse-to-fine map and an evolution law for the CG dynamics. The former can be endowed with great flexibility in discovering appropriate CG variables when combined with deep neural nets. The CG variables identified are not restricted to indicator functions of sub-domains of the state-space as in other generative models [14, 11, 15] and which are difficult to learn when the simulation data are limited and have not sufficiently populated all important regions of the state-space.

The second component pertains to the latent CG evolution law which is learned by employing a large vocabulary of feature functions and sparsity-inducing priors. This leads to interpretable solutions [16], even in the *Small Data* regime that avoid overfitting and reveal salient characteristics of the CG

system [17]. The premise of sparsity [18] has been employed in the past for the discovery of the CG dynamics as e.g. in the SINDy method [19, 20, 21]. This however requires the availability of time-derivatives of the CG variables and does not directly lead to a posterior on the model parameters that can reflect inferential uncertainties. Nonparametric models for the CG dynamics have also been proposed [22] but have been restricted to low-dimensions. The learned CG dynamics are in general nonlinear in contrast to efforts based on transfer operators [23] and the Koopman operators [24, 25, 26] more specifically. While the associated theory guarantees the existence of a linear operator this is possible in the infinite dimensional space of observables, it does not specify how many should be used to obtain a good approximations, and more importantly how one can predict future FG states given predictions on the evolution of those observables i.e. the reconstruction step.

The latter constitutes the main difference of the proposed model with non-generative ones based e.g. on information-theoretic concepts [27, 28, 29] or on the Mori-Zwanzig (MZ) formalism [30, 31, 32]. Apart from the difficulties in approximating the right-hand-side of the MZ-prescribed CG dynamics, and particularly the memory term [33, 34], this can only guarantee correct predictions of the CG variables' evolution. If observables not depending on CG variables are of interest, then a reconstruction operator would need to be added. In contrast, in the proposed model this reconstruction operator is represented by the probabilistic coarse-to-fine map which is simultaneously learned from the data and can quantify predictive uncertainties associated with the information loss that unavoidably takes place in any CG process as well as the fact that finite (and mostly, small) data have been used for training.

The enabling computational technology for training the proposed model is based on probabilistic inference. In order to resolve the intractable posterior on latent variables and model parameters in our Bayesian framework, we make use of Stochastic Variational Inference [35] as MCMC is cumbersome in high dimensions. We operate on the discretized time domain [36] and demonstrate

how amortized [37, 38] and non-amortized approximations can be employed.

The remainder of the paper is structured as follows:

In Section 2 we present the general methodological framework with special attention in the two building blocks of the state-space model proposed i.e. the transition law for the CG dynamics and the incorporation of virtual observables (section 2.2), as well as the emission law which provides the link between CG and FG description through a probabilistic *coarse-to-fine* map (section 2.3). Computational aspects related to inference and prediction are discussed in sections 2.4 and 2.5 respectively. Section 3 contains illustrative applications including coarse-graining, high-dimensional systems of interacting particles (section 3.1) as well as learning the dynamics of a nonlinear pendulum (section 3.2) from a sequence of images. We conclude in section 4 which also contains a discussion on possible extensions.

2. Methodology

In general, we use the subscript 'f' or lower-case letters to denote variables associated with the (high-dimensional) fine-grained(FG)/full-order model and the subscript 'c' or upper-case letters for quantities of the (lower-dimensional) coarse-grained(CG)/reduced-order description. We also use $\hat{\cdot}$ to denote observed quantities. We begin with the presentation of the FG and the CG model and subsequently explain the essential ingredients of the proposed formulation.

2.1. The FG and CG models

We consider a, generally high-dimensional, FG system with state variables \mathbf{x} of dimension d_f ($d_f \gg 1$) such that $\mathbf{x} \in \mathcal{X}_f \subset \mathbf{R}^{d_f}$. The dynamics of the FG system are dictated by system of deterministic or stochastic ODEs i.e.,

$$\dot{\mathbf{x}}_t = \mathbf{f}(\mathbf{x}_t, t) \tag{1}$$

The initial condition \mathbf{x}_0 might be deterministic or drawn from a specified distribution. In the following we do not make explicit use of the FG dynamics but

rely purely on FG data i.e. time sequences simulated from Equation (1) with a time-step, say δt . That is, our observables consists of n data sequences over $m + 1$ FG time-steps δt i.e.,

$$\mathcal{D}_{m,n} = \{\hat{\boldsymbol{x}}_{0:m\delta t}^{(1:n)}\} \quad (2)$$

We denote the (unknown) CG state variables by \mathbf{X} and assume $\mathbf{X} \in \mathcal{X}_c \subset \mathbf{R}^{d_c}$, where d_c is the dimension of the CG system. We presuppose Markovian dynamics¹ for the CG system of the form:

$$\dot{\mathbf{X}}_t = \mathbf{F}(\mathbf{X}_t, t) \quad (3)$$

which we discretize using a linear multistep method and a CG time step Δt as follows:

$$\mathbf{R}_l(\mathbf{X}) = \sum_{k=0}^K (\alpha_k \mathbf{X}_{(l-k)\Delta t} + \Delta t \beta_k \mathbf{F}(\mathbf{X}_{(l-k)\Delta t})) = 0, \quad l = K, K + 1, \dots \quad (4)$$

where α_k, β_k are the parameters of the discretization scheme and \mathbf{R}_l the corresponding residual at time step l [39]. We note that depending on the values of the parameters K, α_k, β_k , several of the well-known, explicit/implicit, numerical time-integration schemes can be recovered. In this work our goal is two-fold:

- a) to identify the CG state-variables \mathbf{X} and their relation with the FG description \boldsymbol{x} ,
- b) to identify the right-hand side of Equation (3),

with the goal of enabling predictions of the FG system over longer time horizons. Traditionally, the aforementioned tasks are *not* considered simultaneously. Usually the CG state variables are specified a priori using domain-knowledge (physical insight) or based on the observables of interest [28]. More recent efforts employ linear or non-linear dimensionality analysis procedures in order to identify a lower-dimensional set of collective variables \mathbf{X} . In both of these

¹As discussed in section 3, this assumption can be relaxed

cases, \mathbf{X} are defined using a *fine-to-coarse*, projection map e.g. $\mathbf{X} = \Pi(\mathbf{x})$ where $\Pi : \mathcal{X}_f \subset \mathbb{R}^{d_f} \rightarrow \mathcal{X}_c \subset \mathbb{R}^{d_c}$. Irrespective of whether this map is prescribed from the physics or learned from data, it is generally a many-to-one function that does not have an inverse i.e. if the CG states \mathbf{X} are known one cannot readily reconstruct \mathbf{x} [40].

We note that that this has nothing to do with the quality of the CG evolution law (problem b) above). Even if the Mori-Zwanzig (MZ) formalism were employed, which in principle provides an exact, closed-system of evolution equations for any observable of the FG states and therefore of $\mathbf{X} = \Pi(\mathbf{x})$, even if all the terms in the right-hand side were available, one would simply be able to predict the future evolution of \mathbf{X} but not \mathbf{x} . This might be sufficient for a lot of problems of practical interest where the CG variables (or observables thereof) are of sole interest. Our goal however is a bit more ambitious, i.e. we seek to find \mathbf{X} and would allow us to reconstruct as accurately as possible the whole FG vector \mathbf{x} into the future. As with any CG process, we recognize that this would unavoidably imply some information loss which in turn will give rise to predictive uncertainty [41]. In this work, we advocate a probabilistic framework that quantifies this uncertainty.

With regards to problem b) above, we note that its solution hinges upon the CG variables \mathbf{X} employed (problem a)). Irrespective of the breadth of the model forms considered (i.e. functions \mathbf{F} in Equation (3)), the evolution of some \mathbf{X} might fall outside this realm. For example, it is known from MZ theory that memory terms can become significant for certain observables. It is well-known that such memory terms can be substituted or approximated by additional variables [42] which. These in turn would imply that an augmented CG description \mathbf{X} in Equation (3) that contains these auxiliary internal state variables [43].

We address problems a) and b) in the coarse-graining process *simultaneously* by employing a probabilistic state-space model. This consists of two densities i.e.

- the transition law which dictates the evolution of the CG variables \mathbf{X} (section 2.2). Special attention is paid to the definition of *virtual observables* with which the CG states and their dynamics can be injected with physical information.
- the emission law which provides the link between CG and FG description through a probabilistic *coarse-to-fine* map [13] (section 2.3).

We emphasize that in our formulation, the CG state-variables \mathbf{X} are implicitly defined as latent generators of the FG description \mathbf{x} . As discussed in detail in the sequel, this enables a straightforward, *probabilistic* reconstruction of \mathbf{x} when \mathbf{X} is known. The inverse map (analogous to Π above) arises naturally through probabilistic inference as explained in section 2.4. An overview of the essential elements of the proposed model can be seen in the probabilistic graphical model in Figure 1.

2.2. Transition Law: CG dynamics and virtual observables

Typical state-space models [44, 45, 46, 37] postulate Markovian, stochastic dynamics for the hidden variables \mathbf{X} , in the form of a diffusion process, which are subsequently discretized *explicitly* using e.g. a Euler-Maruyama scheme with time step Δt . This gives rise to a, generally Gaussian, conditional density $p(\mathbf{X}_{(l+1)\Delta t}|\mathbf{X}_{l\Delta t})$ which can be stacked over multiple time-instants in order to formulate a generalized prior on the CG-space.

When the CG state-variables \mathbf{X} are given physical meaning (e.g. as thermodynamic state variables), then some of the equations for their evolution are prescribed by associated physical principles e.g. conservation of mass, momentum, energy. These can be reflected in the residuals of the governing equations as in Equation (4) or more generally as equality constraints of the form:

$$\mathbf{c}_l(\mathbf{X}_{l\Delta t}) = \mathbf{0}, \quad l = 0, 1, \dots \quad (5)$$

which must hold at each time-step. The function $\mathbf{c}_l : \mathcal{X}_c \subset \mathbb{R}^{d_c} \rightarrow \mathbb{R}^{M_c}$ enforces these known constraints at each time-step (see specific examples in section 3) and

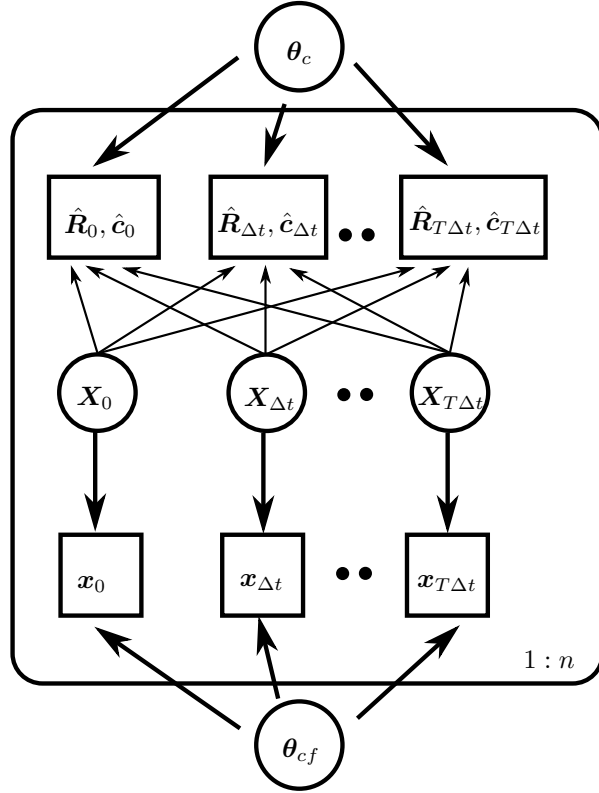


Figure 1: Proposed probabilistic graphical model. The CG variables \mathbf{X} are latent and are inferred together with the parameters θ_c and θ_{cf} . Apart from the the FG states \mathbf{x} , the observables are augmented by *virtual observables* $\hat{\mathbf{R}}, \hat{\mathbf{c}}$ (see section 2.2)

the only requirement we will impose is that of differentiability of \mathbf{c}_l (see section 2.4). In order to account for the aforementioned constraints in the transition law of the CG state variables, we employ a novel (to the best of our knowledge) concept of *virtual observables*. In particular for each of the constraints \mathbf{R}_l in Equation (4), we define a new variable/vector $\hat{\mathbf{R}}_l$ which relates to \mathbf{R}_l as follows:

$$\hat{\mathbf{R}}_l = \mathbf{R}_l(\mathbf{X}) + \sigma_R \boldsymbol{\epsilon}_R, \quad \boldsymbol{\epsilon}_R \sim \mathcal{N}(\mathbf{0}, \mathbf{I}) \quad (6)$$

We further assume that $\hat{\mathbf{R}}_l$ have been *virtually observed* and $\hat{\mathbf{R}}_l = \mathbf{0}$ leading to an augmented version of the data in Equation (2), by a set of virtual observations and therefore virtual likelihoods of the type:

$$p(\hat{\mathbf{R}}_l = \mathbf{0} | \mathbf{X}, \sigma_R) = \mathcal{N}(\mathbf{0} | \mathbf{R}_l(\mathbf{X}), \sigma_R^2 \mathbf{I}) \quad (7)$$

The "noise" parameter σ_R determines the intensity of the enforcement of the virtual observations and is analogous to the tolerance parameter with which residuals are enforced in a deterministic solution of the dynamics. Similarly, for constraints of the form of Equation (5), additional variables and virtual observables of the type:

$$\mathbf{0} = \hat{\mathbf{c}}_l = \mathbf{c}_l(\mathbf{X}_{l\Delta t}) + \sigma_c \boldsymbol{\epsilon}_c, \quad \boldsymbol{\epsilon}_c \sim \mathcal{N}(\mathbf{0}, \mathbf{I}) \quad (8)$$

can be defined which would lead to an augmented (virtual) likelihood with terms of the type:

$$p(\hat{\mathbf{c}}_l = \mathbf{0} | \mathbf{X}_{l\Delta t}, \sigma_c) = \mathcal{N}(\mathbf{0} | \mathbf{c}_l(\mathbf{X}_{l\Delta t}), \sigma_c^2 \mathbf{I}) \quad (9)$$

In the following, as the goal is to identify the right-hand side of the evolution laws in Equation (3), we denote by $\boldsymbol{\theta}_c$ the parameters appearing in \mathbf{F} i.e. $\mathbf{F}(\mathbf{X}_t, t; \boldsymbol{\theta}_c)$. Accordingly, the virtual observations in Equation (6) or Equation (8) would depend on $\boldsymbol{\theta}_c$. We defer to section 3, a detailed discussion on the form, the parametrization as well as the prior specifications in the Bayesian setting adopted. The latter plays an important role as with sparsity-inducing priors we can avoid overfitting and obtain a parsimonious and physically-interpretable solution for \mathbf{F} [13].

Observables \mathcal{D}	$\hat{\mathbf{x}}_{0:T\Delta t}^{(1:n)}$	FG simulation Data
	$\hat{\mathbf{R}}_{0:T}^{(1:n)}$	Virtual observables corresponding to CG model residuals
	$\hat{\mathbf{c}}_{0:T}^{(1:n)}$	Virtual Observables corresponding to CG constraints
Latent variables	$\mathbf{X}_{0:T\Delta t}^{(1:n)}$	CG state variable
Model parameters θ	θ_{cf}	parameters in the coarse-to-fine mapping
	θ_c	parameters in the CG evolution law

Table 1: Data, latent variables and model parameters

2.3. Emission law: Coarse-to-Fine map

As discussed previously, we adopt a probabilistic *generative* model in the definition of the CG state-variables through a *coarse-to-fine* map [13] as opposed to traditional, many-to-one maps from the FG description to the CG one. We denote the associated (conditional) density by:

$$p_{cf}(\mathbf{x}_t | \mathbf{X}_t; \theta_{cf}) \quad (10)$$

where θ_{cf} denote the (unknown) parameters that will be learned from the data. The particular form of p_{cf} can be adapted to the particulars of the problem and can be endowed with various levels of domain knowledge. In section 3, we provide various examples from particle-systems where p_{cf} is fully determined by the physics, to a more abstract example where deep neural networks are employed in order to learn the full p_{cf} . We note finally that a (probabilistic) fine-to-coarse map can still be learned in the current setting, and would correspond to the *posterior* of \mathbf{X}_t given \mathbf{x}_t . We discuss this as well as all aspects pertaining to inference and learning in the next section.

2.4. Inference and Learning

We start this section by summarizing the main elements of the model presented (i.e. data, latent variables and parameters - see also Table 1) and subsequently describe a fully Bayesian inference scheme based on Stochastic Variational Inference (SVI, [35]) tools.

We adopt an enlarged definition of *data* which we cumulatively denote by \mathcal{D} and which encompasses:

- FG simulation data as in Equation (2) consisting of n sequences of the FG state-variables. As the likelihood model implied by the p_{cf} in Equation (10) involves only the observables at each *coarse* time-step we denote those by $\{\hat{\mathbf{x}}_{0:T\Delta t}^{(1:n)}\}$. We assume that the number of observations in each sequence is the same although this is not necessary. In fact the length of each time-sequence and the number of time-sequences needed could be the subject of an active learning scheme. This could be particularly important in cases where very expensive, high-dimensional FG simulators are employed. Naturally, the proposed formulation can account for any type of (in)direct or (in)complete experimental observations relating to FG states which we omit here for simplicity of the presentation.
- Virtual observables at each time-step l consisting of residuals $\hat{\mathbf{R}}_l^{(1:n)}$ as in Equation (6) and/or constraints $\hat{\mathbf{c}}_l^{(1:n)}$ as in Equation (8) (the superscript pertains to the time sequence $i = 1, \dots, n$). Assuming they pertain to all time-steps, we denote them by $\{\hat{\mathbf{R}}_{0:T}^{(1:n)}, \hat{\mathbf{c}}_{0:T}^{(1:n)}\}$. We assume these virtual observations pertain to one or more time-steps indexed by l and to n time sequences.

The latent (unobserved) variables of the model are represented by the CG state-variables $\{\mathbf{X}_{0:T\Delta t}^{(1:n)}\}$ which relate to the FG data through the p_{cf} (in Equation (10)) and to the virtual observables through Equation (7) or Equation (9).

Finally, the (unknown) parameters of the model which we denote cumulatively by $\boldsymbol{\theta}$ consist of²:

- $\boldsymbol{\theta}_c$ which parametrize the right-hand-side of the CG evolution law (see end of section 2.2),
- $\boldsymbol{\theta}_{cf}$ which parametrize the probabilistic coarse-to-fine map (Equation (10)),

²If any of the parameters in this list are prescribed, then they are omitted from $\boldsymbol{\theta}$.

- σ_R, σ_c involved in the enforcement of virtual observables in Equation (6) and Equation (8) respectively, and,
- *hyperparameters* associated with the priors employed on the latent variables or the previous parameters.

Following a fully-Bayesian formulation, we can express the posterior of the unknowns (i.e. latent variables and parameters) as follows:

$$p(\mathbf{X}_{0:T\Delta t}^{(1:n)}, \boldsymbol{\theta} | \mathcal{D}) = \frac{p(\mathcal{D} | \mathbf{X}_{0:T\Delta t}^{(1:n)}, \boldsymbol{\theta}) p(\mathbf{X}_{0:T\Delta t}^{(1:n)}, \boldsymbol{\theta})}{p(\mathcal{D})} \quad (11)$$

where $p(\mathbf{X}_{0:T\Delta t}^{(1:n)}, \boldsymbol{\theta})$ denotes the prior on the latent variables and parameters.

We discuss first the likelihood term $p(\mathcal{D} | \mathbf{X}_{0:T\Delta t}^{(1:n)}, \boldsymbol{\theta})$ which can be decomposed into the product of three (conditionally) independent terms, one for each data-type, i.e.:

$$p(\mathcal{D} | \mathbf{X}_{0:T\Delta t}^{(1:n)}, \boldsymbol{\theta}) = p(\hat{\mathbf{x}}_{0:T\Delta t}^{(1:n)} | \mathbf{X}_{0:T\Delta t}^{(1:n)}, \boldsymbol{\theta}) p(\hat{\mathbf{R}}_{0:T}^{(1:n)} | \mathbf{X}_{0:T\Delta t}^{(1:n)}, \boldsymbol{\theta}) p(\hat{\mathbf{c}}_{0:T}^{(1:n)} | \mathbf{X}_{0:T\Delta t}^{(1:n)}, \boldsymbol{\theta}) \quad (12)$$

We further note that (from Equation (10)):

$$p(\hat{\mathbf{x}}_{0:T\Delta t}^{(1:n)} | \mathbf{X}_{0:T\Delta t}^{(1:n)}, \boldsymbol{\theta}) = \prod_{i=1}^n \prod_{l=0}^T p_{cf}(\mathbf{x}_{l\Delta t}^{(i)} | \mathbf{X}_{l\Delta t}^{(i)}, \boldsymbol{\theta}_{cf}) \quad (13)$$

and (from Equation (7)):

$$p(\hat{\mathbf{R}}_{0:T}^{(1:n)} | \mathbf{X}_{0:T\Delta t}^{(1:n)}, \boldsymbol{\theta}) = \prod_{i=1}^n \prod_{l=0}^T \mathcal{N}(\mathbf{0} | \mathbf{R}_l(\mathbf{X}^{(i)}), \sigma_R) \propto \prod_{i=1}^n \prod_{l=0}^T \frac{1}{\sigma_R^{\dim(\mathbf{R})}} \exp\left\{-\frac{1}{2\sigma_R^2} \|\mathbf{R}_l(\mathbf{X}^{(i)})\|^2\right\} \quad (14)$$

and (from Equation (9)):

$$p(\hat{\mathbf{c}}_{0:T}^{(1:n)} | \mathbf{X}_{0:T\Delta t}^{(1:n)}, \boldsymbol{\theta}) = \prod_{i=1}^n \prod_{l=0}^T \mathcal{N}(\mathbf{0} | \mathbf{c}_l(\mathbf{X}_{l\Delta t}^{(i)}), \sigma_R) \propto \prod_{i=1}^n \prod_{l=0}^T \frac{1}{\sigma_R^{\dim(\mathbf{R})}} \exp\left\{-\frac{1}{2\sigma_R^2} \|\mathbf{c}_l(\mathbf{X}_{l\Delta t}^{(i)})\|^2\right\} \quad (15)$$

While the complexity of the terms involved imply a non-analytic solution for the posterior, we emphasize that the terms above encode actual and virtual observables (constraints) and they are differentiable, a property that is crucial for carrying out Variational Inference.

Before presenting the inference procedure, we mention an interesting possibility for encoding prior information for the latent CG states $\mathbf{X}_{0:T\Delta t}^{(1:n)}$ through the prior term $p(\mathbf{X}_{0:T\Delta t}^{(1:n)})$. A desirable property of the CG state-variables is that of *slowness* i.e. that they should capture features of the system that exhibit (much) larger time-scales [47]. The discovery of such features has been the goal of several statistical analysis procedures (e.g. Slow Feature Analysis [48]) as well as in physics/chemistry literature (see a recent review in [23]). In this work we promote the discovery of such slow features by appropriate prior selection and in particular by penalizing the jumps two successive time-instants, i.e.:

$$\begin{aligned}
p(\mathbf{X}_{0:T\Delta t}^{(1:n)}) &= \prod_{i=1}^n p_{c,0}(\mathbf{X}_0^{(i)}) \prod_{l=0}^{T-1} p(\mathbf{X}_{(l+1)\Delta t}^{(i)} | \mathbf{X}_{l\Delta t}^{(i)}, \sigma_X^2 \mathbf{I}) \\
&= \prod_{i=1}^n p_{c,0}(\mathbf{X}_0^{(i)}) \prod_{l=0}^{T-1} \mathcal{N}(\mathbf{X}_{(l+1)\Delta t}^{(i)} | \mathbf{X}_{l\Delta t}^{(i)}, \sigma_X^2 \mathbf{I}) \\
&\propto \prod_{i=1}^n p_{c,0}(\mathbf{X}_0^{(i)}) \prod_{l=0}^{T-1} \frac{1}{\sigma_X^{dc}} \exp\left\{-\frac{1}{\sigma_X^2} \left| \mathbf{X}_{(l+1)\Delta t}^{(i)} - \mathbf{X}_{l\Delta t}^{(i)} \right|^2\right\}
\end{aligned} \tag{16}$$

where $p_{c,0}$ is a prior density for the initial CG state. We observe that the strength of the penalty is inversely proportional to the hyperparameter σ_X^2 and in the limit $\sigma_X^2 \rightarrow 0$ it implies a constant time history of \mathbf{X}_t . As the appropriate value for σ_X^2 depends on the problem, we include this in the parameter vector $\boldsymbol{\theta}$ that is inferred/learned from the data.

Given the intractability of the actual posterior, we employ in this work Variational Inference. This operates on a parameterized family of densities, say $q_\phi(\mathbf{X}_{0:T\Delta t}^{(1:n)}, \boldsymbol{\theta})$ and attempts to find the one (i.e. the value of ϕ) that most closely approximates the posterior by minimizing their Kullback-Leibler divergence. It can be readily shown [49], that the optimal q_ϕ , maximizes the

Evidence Lower Bound (ELBO) $\mathcal{F}(q_\phi(\mathbf{X}_{0:T\Delta t}^{(1:n)}, \boldsymbol{\theta}))$ below:

$$\begin{aligned}
\log p(\mathcal{D}) &= \log \int p(\mathcal{D}, \mathbf{X}_{0:T\Delta t}^{(1:n)}, \boldsymbol{\theta}) d\mathbf{X}_{0:T\Delta t}^{(1:n)} d\boldsymbol{\theta} \\
&= \log \int \frac{p(\mathcal{D} | \mathbf{X}_{0:T\Delta t}^{(1:n)}, \boldsymbol{\theta}) p(\mathbf{X}_{0:T\Delta t}^{(1:n)}, \boldsymbol{\theta})}{q_\phi(\mathbf{X}_{0:T\Delta t}^{(1:n)}, \boldsymbol{\theta})} q_\phi(\mathbf{X}_{0:T\Delta t}^{(1:n)}, \boldsymbol{\theta}) d\mathbf{X}_{0:T\Delta t}^{(1:n)} d\boldsymbol{\theta} \\
&\geq \int \log \frac{p(\mathcal{D} | \mathbf{X}_{0:T\Delta t}^{(1:n)}, \boldsymbol{\theta}) p(\mathbf{X}_{0:T\Delta t}^{(1:n)}, \boldsymbol{\theta})}{q_\phi(\mathbf{X}_{0:T\Delta t}^{(1:n)}, \boldsymbol{\theta})} q_\phi(\mathbf{X}_{0:T\Delta t}^{(1:n)}, \boldsymbol{\theta}) d\mathbf{X}_{0:T\Delta t}^{(1:n)} d\boldsymbol{\theta} \\
&= \mathcal{F}(q_\phi(\mathbf{X}_{0:T\Delta t}^{(1:n)}, \boldsymbol{\theta}))
\end{aligned} \tag{17}$$

In the examples analyzed we decompose the approximate posterior as:

$$\begin{aligned}
q_\phi(\mathbf{X}_{0:T\Delta t}^{(1:n)}, \boldsymbol{\theta}) &= q_\phi(\mathbf{X}_{0:T\Delta t}^{(1:n)}) q_\phi(\boldsymbol{\theta}) \\
&= \prod_{i=0}^n q_\phi(\mathbf{X}_{0:T\Delta t}^{(i)}) q_\phi(\boldsymbol{\theta})
\end{aligned} \tag{18}$$

where the first line is the so-called mean-field approximation and the second is a direct consequence of the (conditional) independence of the time sequences in the likelihood. We note that evaluations of the ELBO \mathcal{F} involves expectations with respect to q_ϕ i.e.:

$$\mathcal{F}(q_\phi(\mathbf{X}_{0:T\Delta t}^{(1:n)}, \boldsymbol{\theta})) = \mathbb{E}_{q_\phi} \left[\log p(\mathcal{D} | \mathbf{X}_{0:T\Delta t}^{(1:n)}, \boldsymbol{\theta}) \right] + \mathbb{E}_{q_\phi} \left[\log \frac{p(\mathbf{X}_{0:T\Delta t}^{(1:n)}, \boldsymbol{\theta})}{q_\phi(\mathbf{X}_{0:T\Delta t}^{(1:n)}, \boldsymbol{\theta})} \right] \tag{19}$$

and in order to maximize it (with respect to ϕ), gradients of those are needed. Given the intractability of these expectations and their derivatives, we employ Monte Carlo estimates in combination with stochastic gradient ascent for the ϕ -updates. In order to reduce the Monte Carlo error in these estimates, we make use of the reparametrization trick [50], for which the differentiability of the residuals/constraints is necessary. We specify the particulars of the algorithm more precisely in the numerical illustration section (see e.g. Algorithm 3 or 4).

We note that maximum likelihood or maximum-a-posteriori (MAP) point estimates for any of the parameters involved can be obtained as a special case of the aforementioned scheme by employing a q_ϕ that is equal to a Dirac-delta function. Furthermore, amortized versions of the approximate posterior q_ϕ i.e. forms that explicitly account on the dependence on the data values, can be

employed in part or in whole. These have the capability of being able to transfer information across data points and are necessary in the realm of Big Data. We note though that we operate in the *Small Data* regime, i.e. the number of time sequences n (and time-steps T) is not particularly large. Hybrid versions between amortized and non-amortized posteriors could also be employed [51]. Finally, the scalability of the presented methods of variational inference could be increased as described in [52]. This could be beneficial especially for large-scale problems.

2.5. Prediction

An essential feature of the proposed algorithm is the ability to produce *probabilistic* predictive estimates. These encompass the information-loss due to the coarse-graining process as well as the epistemic uncertainty arising from finite (and small) datasets. We distinguish between two settings:

- a) predictions into the future of a sequence i observed up to time-step T i.e. $\hat{\mathbf{x}}_{0:T\Delta t}^{(i)}$ which was used in the training phase ("interpolative" setting - see section 3), or
- b) predictions into the future for a completely new initial condition $\hat{\mathbf{x}}_0$ ("extrapolative" setting - see section 3).

We note that any predictions should account for the domain knowledge incorporated in the training through the residuals \mathbf{R}_l or constraints \mathbf{c}_l . Formally that is, one should enlarge the posterior density defined in Equation (11), in order to account for the residuals and/or constraints at future time-steps. This would in turn imply, that future (FG or CG) states should be inferred from such an augmented posterior i.e. prediction would imply an enlarged inference process. In the examples presented we adopt a simpler procedure that retains the essential features (i.e. probabilistic nature) but is more computationally expedient. In particular for case a) above if $q_\phi(\mathbf{X}_{T\Delta t}^{(i)})$ is the (marginal) posterior

of the last, hidden CG state and $q(\boldsymbol{\theta})$ the posterior of the model parameters, then we (see also Algorithm 1):

- sample from $q(\mathbf{X}_{T \Delta t}^{(i)}), q(\boldsymbol{\theta})$
- for each sample, we propagate the CG dynamics dynamics of Equation (3) (e.g. by solving the corresponding residual Equations (4)) in order to obtain $\mathbf{X}_{(T+1) \Delta t}^{(i)}, \mathbf{X}_{(T+2) \Delta t}^{(i)}, \dots$, and,
- we sample $\mathbf{x}_{(T+1) \Delta t}^{(i)}$ from $p_{cf}(\mathbf{x}_{(T+1) \Delta t}^{(i)} | \mathbf{X}_{(T+1) \Delta t}^{(i)}, \boldsymbol{\theta}_{cf})$, $\mathbf{x}_{(T+2) \Delta t}^{(i)}$ from $p_{cf}(\mathbf{x}_{(T+2) \Delta t}^{(i)} | \mathbf{X}_{(T+2) \Delta t}^{(i)}, \boldsymbol{\theta}_{cf})$ etc.

We note that this procedure does not necessarily ensure enforcement of the constraints by future CG states but gives rise to samples of the full FG state evolution from which any observable of interest as well as the predictive uncertainty can be computed.

Algorithm 1: Prediction-Algorithm Case a)

Result: Samples of $\mathbf{x}_{(T+P)\Delta t}^{(i)}$

Data: $q_\phi(\mathbf{X}_T \Delta t), q_\phi(\boldsymbol{\theta})$

- 1 Sample from $q_\phi(\mathbf{X}_T \Delta t)$ and $q_\phi(\boldsymbol{\theta})$;
 - 2 **while** *Time-step $(T + P)\Delta t$ of interest not reached* **do**
 - 3 | Apply the CG evolution law as described in Equation (4);
 - 4 **end**
 - 5 Sample from $p_{cf}(\mathbf{x}_{(T+P) \Delta t} | \mathbf{X}_{(T+P) \Delta t}, \boldsymbol{\theta})$
-

For case b) above, i.e. for a new FG initial condition $\hat{\mathbf{x}}_0$, the evolution equations of the CG states as well as the emission density p_{cf} can be employed as long as the initial state \mathbf{X}_0 is specified or better yet inferred. For that purpose the posterior $p(\mathbf{X}_0 | \hat{\mathbf{x}}_0)$ of \mathbf{X}_0 need to be determined which according to Bayes rule will be proportional to:

$$p(\mathbf{X}_0 | \hat{\mathbf{x}}_0) \propto p_{cf}(\hat{\mathbf{x}}_0 | \mathbf{X}_0, \boldsymbol{\theta}_{cf}) p_{c,0}(\mathbf{X}_0) \quad (20)$$

where $p_{c,0}(\mathbf{X}_0)$ is the initial state's prior (see also Equation (16)). For each sample of $\boldsymbol{\theta}_{cf}$ from the (approximate) posterior $q_\phi(\boldsymbol{\theta}_{cf})$, samples of \mathbf{X}_0 must

be drawn from $p(\mathbf{X}_0|\hat{\mathbf{x}}_0)$ and subsequently propagated as in the 3 steps above in order to obtain predictive samples of the full FG state vector (see Algorithm 2).

Algorithm 2: Prediction-Algorithm Case b)

Result: Samples of $\mathbf{x}_{P\Delta t}$

Data: $p_\phi(\hat{\mathbf{x}}_0), q_\phi(\boldsymbol{\theta})$

- 1 Apply Bayesian Inference as described in Equation (20) to infer $p(\mathbf{X}_0|\hat{\mathbf{x}}_0)$;
 - 2 Sample from $p(\mathbf{X}_0|\hat{\mathbf{x}}_0)$ and $q(\boldsymbol{\theta})$;
 - 3 **while** *Time-step $P\Delta t$ of interest not reached* **do**
 - 4 | Apply the CG evolution law as described in Equation (4);
 - 5 **end**
 - 6 Sample from $p_{cf}(\mathbf{x}_{P\Delta t}|\mathbf{X}_{P\Delta t}, \boldsymbol{\theta})$
-

3. Numerical Illustrations

We demonstrate the capabilities of the proposed framework in discovering predictive, coarse-grained evolution laws as well as effective coarse-grained descriptions, on three examples. Two of those involve very high-dimensional systems of stochastically interacting particles (section 3.1, [13]) and the third, a nonlinear pendulum, the dynamics of which we attempt to identify simply from sequences of images (section 3.2, [21]). In the sequel, we specify the elements of the proposed model that were presented generically in the previous sections and concretize parametrizations and their meaning. The goals of the numerical illustrations are:

- to assess the predictive performance of the model under "interpolative" and "extrapolative" conditions. By "interpolative" we mean the ability to predict the evolution of an FG states-sequence when data from this sequence has been used for training. By "extrapolative", we mean the ability to predict the full FG state evolution from new initial conditions that were *not* used in training.

- to examine the effect of the datasize n and assess the model’s ability to learn the correct structure with small n .
- to examine the enforcement of the residuals/constraints (e.g. conservation of mass) in inference and predicted states.
- to examine the ability of the model to identify *sparse*, interpretable solutions for the CG dynamics.
- to assess the magnitude and time evolution of the predictive uncertainty estimates.
- to assess the ability of the model in learning effective CG state variables and accurate coarse-to-fine maps.

Some of the simulation results as well as the corresponding code will be made available at the following [github repository](#) upon publication.

3.1. Particle systems

3.1.1. FG model

The FG model consists of d_f identical particles which can move in the bounded one-dimensional domain $[-1, 1]$ (under periodic boundary conditions). The FG variables \mathbf{x}_t consist therefore of the coordinates of the particles at each time instant t and therefore the dimension of the system d_f is equal to the number of particles. We consider two types of stochastic dynamics that correspond to an advection-diffusion-type (section 3.1.4) and an inviscid-Burgers-type behavior (section 3.1.5). The particulars of the microscopic dynamics are described in the corresponding sections. In the following, we discuss common aspects of both problems that pertain to the CG description, the CG evolution law and the inference procedures.

3.1.2. CG model, associated densities and virtual observables

For the CG representation, we employ the normalized particle density $\rho(s, t)$, $s \in [-1, 1]$ [53] which we discretize in d_c bins. The state vector $\mathbf{X}_t = \{X_{t,j}\}_{j=1}^{d_c}$

contains the particle density values in each of the bins j , i.e. $\sum_{j=1}^{d_c} X_{t,j} = 1$ and $X_{t,j} \geq 0 \forall t, j$.

The nature of the CG variables \mathbf{X}_t suggests a *multinomial* for the coarse-to-fine density p_{cf} (section 2.3) i.e.:

$$p_{cf}(\mathbf{x}_t | \mathbf{X}_t) = \frac{d_f!}{m_1(\mathbf{x}_t)! m_2(\mathbf{x}_t)! \dots m_{d_c}(\mathbf{x}_t)!} \prod_{j=1}^{d_c} X_{t,j}^{m_j(\mathbf{x}_t)}, \quad (21)$$

where $m_j(\mathbf{x}_t)$ is the number of particles in bin j . The underlying assumption is that, given the CG state \mathbf{X}_t , the coordinates of the particles \mathbf{x}_t are *conditionally* independent which does *not* imply that they move independently nor that they cannot exhibit coherent behavior [13]. The practical consequence of Equation (21) is that no parameters need to be learned for p_{cf} (in contrast to section 3.2).

With regards to the evolution law of the CG states (Equation (3)), we postulate a right-hand side $\mathbf{F}(\mathbf{X}_t; \boldsymbol{\theta}_c) = \{F_j(\mathbf{X}_t; \boldsymbol{\theta}_c)\}_{j=1}^{d_c}$ of the form:

$$\begin{aligned} F_j(\mathbf{X}_t, \boldsymbol{\theta}_c) &= \sum_{m=1}^M \theta_{c,m} \psi_m^{(j)}(\mathbf{X}_t) \\ &= \underbrace{\sum_{h=-}^H \theta_{c,h}^{(1)} X_{t,j+h}}_{1^{st} \text{ order}} + \underbrace{\sum_{h_1=-H}^H \sum_{h_2 \geq h_1}^H \theta_{c, (h_1, h_2)}^{(2)} X_{t,j+h_1} X_{t,j+h_2}}_{2^{nd} \text{ order}} \end{aligned} \quad (22)$$

which consists of first- and second-order interactions over a window of size H with $\boldsymbol{\theta}_c^{(1)}$ and $\boldsymbol{\theta}_c^{(2)}$ denoting the vectors of the corresponding unknown coefficients. In this case, the total number of unknown coefficients $\boldsymbol{\theta}_c$, is $M = \dim(\boldsymbol{\theta}_c) = (2H + 1) + (H + 1)(2H + 1)$ and grows quadratically with the neighborhood-size H . Naturally higher-order interactions or even feature functions of non-polynomial type could also be employed. Non-Markovian models could be accommodated as well by accounting for memory terms. It is obviously impossible to know a priori which feature functions are relevant in the evolution of the CG states or what types of interactions are essential (e.g. first, second-order etc). At the same time, and especially in the Small Data regime considered, employing a large vocabulary of feature functions can lead to *overfitting*, lack of interpretability and poor predictions, particularly under "extrap-

relative” conditions. This highly-important *model selection* issue has been of concern in several coarse-graining studies [54]. We propose of automatically addressing this within the Bayesian framework advocated by employing appropriate sparsity-inducing priors for $\boldsymbol{\theta}_c$ [13]. In particular, we make use of the Automatic Relevance Determination (ARD, [55]) model according to which

$$p(\boldsymbol{\theta}_{c,m} | \tau_m) = \mathcal{N}(\boldsymbol{\theta}_{c,m} | \mathbf{0}, \tau_m^{-1}) \quad (23)$$

with the following hyperprior for the precision hyperparameters $\boldsymbol{\tau} = \{\tau_m\}_{m=1}^M$:

$$p(\tau_m | \gamma_0, \delta_0) = \text{Gamma}(\tau_m | \gamma_0, \delta_0) \quad (24)$$

The hyperparameters γ_0 and δ_0 are set to very small values 10^{-9} in all ensuing studies [56]. As we demonstrate in the sequel, the hyperprior proposed can give rise to parsimonious solutions for the CG dynamics even in the Small Data setting considered.

A discretized version of the CG evolution law (Equation (3) and Equation (22)) with time step Δt is considered by employing a forward Euler scheme³ which implies the following residual vector \mathbf{R}_l at each time-step l (Equation (4)):

$$\mathbf{R}_l(\mathbf{X}) = \mathbf{X}_{(l+1)\Delta t, j} - \mathbf{X}_{l\Delta t, j} - \Delta t \mathbf{F}(\mathbf{X}_{l\Delta t, j}, \boldsymbol{\theta}_c), \forall l \quad (25)$$

and the corresponding virtual observables $\hat{\mathbf{R}}_l$ (Equation (6)).

More importantly, the nature of the CG variables suggests a *conservation of mass* constraint that has to be fulfilled at each time step l . In view of the discussion of section 2.2, this suggests the scalar constraint function Equation (5):

$$c_l(\mathbf{X}_{l\Delta t}) = \sum_{j=1}^{d_c} X_{l\Delta t, j} - 1 = 0, \quad \forall l \quad (26)$$

and the corresponding virtual observables \hat{c}_l (Equation (8)).

³This corresponds to a multistep method in Equation (4) with $K = 1$, $a_0 = 1, a_1 = -1, \beta_0 = 0, \beta_1 = -1$

3.1.3. Inference and Learning

Given the multinomial p_{cf} in Equation (21), we employed the following procedure for generating training data which consists of n numerical experiments in which the FG model is randomly initialized and propagated for one coarse time-step Δt i.e. for $\frac{\Delta t}{\delta t}$ microscopic time-steps. In particular:

- For $i = 1, \dots, n$, we:
 - sample CG initial state $\hat{\mathbf{X}}_0^{(i)}$ from a density $p_{c,0}(\hat{\mathbf{X}}_0^{(i)})$.
 - sample FG initial state $\hat{\mathbf{x}}_0^{(i)}$ from $p_{cf}(\hat{\mathbf{x}}_0^{(i)} | \mathbf{X}_0^{(i)})$.
 - solve the (discretized) FG model for $\frac{\Delta t}{\delta t}$ microscopic time-steps and record final state $\hat{\mathbf{x}}_{\Delta t}^{(i)}$

The generated FG data $\{\hat{\mathbf{x}}_{\Delta t}^{(i)}\}_{i=1}^n$ over a *single* CG time-step are used subsequently to draw inferences on the CG model states and parameters (section 2.4). We note that longer time sequences could readily be generated (albeit at an increased cost). The number of samples n is also something that can be selected adaptively since inferences and predictions can be updated as soon as more data become available. The density $p_{c,0}(\mathbf{X}_0^{(i)})$ from which initial CG states are drawn, can be selected quite flexibly and some indicative samples are shown in Figure 2 for the advection-diffusion case, and in Figure 12 for the inviscid-Burgers case. In summary, the data \mathcal{D} employed, apart from $\{\hat{\mathbf{x}}_{\Delta t}^{(i)}\}_{i=1}^n$ above consists of the virtual observables $\{\hat{\mathbf{R}}_0^{(1:n)}, \hat{\mathbf{c}}_1^{(1:n)}\}$.

As a result of the data employed and the parametrization adopted, we have $\mathbf{X}_{\Delta t}^{(1:n)}$ as the sole latent vector and $\boldsymbol{\theta}_c, \boldsymbol{\tau}$ as the unknown (hyper)parameters. Due to considering only a single CG time-step, we omitted the slowness prior (see Equation (16)). Hence we sought an approximate posterior $q_\phi(\mathbf{X}_{\Delta t}, \boldsymbol{\theta}_c, \boldsymbol{\tau})$ (Equation (17)) which we factorized as in Equation (18) as follows:

$$q_\phi(\mathbf{X}_{\Delta t}^{(1:n)}, \boldsymbol{\theta}_c, \boldsymbol{\tau}) = \prod_{i=1}^n q_\phi(\mathbf{X}_{\Delta t}^{(i)})q(\boldsymbol{\theta}_c)q(\boldsymbol{\tau}) \quad (27)$$

Upon substitution in Equation (19), this yields the following ELBO:

$$\begin{aligned} \mathcal{F}(q_\phi(\mathbf{X}_{\Delta t}^{(1:n)}, \boldsymbol{\theta}_c, \boldsymbol{\tau})) &= \mathbb{E}_{q_\phi} [\log p(\mathcal{D} | \mathbf{X}_{\Delta t}^{(1:n)}, \boldsymbol{\theta}_c)] + \mathbb{E}_{q_\phi} [\log p(\boldsymbol{\theta}_c | \boldsymbol{\tau})] \\ &\quad + \mathbb{E}_{q_\phi} [\log p(\boldsymbol{\tau})] - \mathbb{E}_{q_\phi} [\log q_\phi] \end{aligned} \quad (28)$$

where:

$$p(\mathcal{D} | \mathbf{X}_{\Delta t}^{(1:n)}, \boldsymbol{\theta}_c) = p(\hat{\mathbf{x}}_{\Delta t}^{(1:n)} | \mathbf{X}_{\Delta t}^{(1:n)}) p(\hat{\mathbf{R}}_0^{(1:n)} | \mathbf{X}_{\Delta t}^{(1:n)}, \boldsymbol{\theta}_c) p(\hat{\mathbf{c}}_1^{(1:n)} | \mathbf{X}_{\Delta t}^{(1:n)}) \quad (29)$$

Based on Equation (28) the optimal variational posterior densities can be obtained as:

$$\log q^{opt}(\boldsymbol{\theta}_c) = \mathbb{E}_{q_\phi(\mathbf{X}_{\Delta t}^{(1:n)})} [\log(p(\hat{\mathbf{R}}_0^{(1:n)} | \mathbf{X}_{0:1\Delta t}^{(1:n)}, \boldsymbol{\theta}_c))] + \mathbb{E}_{q(\boldsymbol{\tau})} [\log(p(\boldsymbol{\theta}_c | \boldsymbol{\tau}))] \quad (30)$$

$$\log q^{opt}(\boldsymbol{\tau}) = \mathbb{E}_{q_\phi(\boldsymbol{\theta}_c)} [\log(p(\boldsymbol{\theta}_c | \boldsymbol{\tau}))] + \log(p(\boldsymbol{\tau})) \quad (31)$$

$$\log q_\phi^{opt}(X_{\Delta t}^{(i)}) = \log(p_{cf}(\mathbf{x}_{\Delta t}^i | \mathbf{X}_{\Delta t}^i) + \mathbb{E}_{q_\phi(\boldsymbol{\theta}_c)} [\log(p(\hat{\mathbf{R}}_0^{(i)} | \mathbf{X}_{0:1\Delta t}^{(i)}, \boldsymbol{\theta}_c))] + \log(p(\hat{\mathbf{c}}_1^{(i)} | \mathbf{X}_{\Delta t}^{(i)})) \quad (32)$$

Although the equations above are coupled, a closed-form solution can be obtained for the first two of them. In particular, the optimal posterior approximation for $\boldsymbol{\theta}_c$ is a multivariate normal with mean $\boldsymbol{\mu}_{\boldsymbol{\theta}_c}$ and covariance $\mathbf{S}_{\boldsymbol{\theta}_c}$.

$$\mathbf{S}_{\boldsymbol{\theta}_c}^{-1} = \sigma_R^{-2} \sum_{i=1}^n \sum_{j=1}^{d_c} \mathbb{E}_{q_\phi(\mathbf{X}_{\Delta t}^{(i)})} [\boldsymbol{\psi}^{(j)}(\mathbf{X}_{\Delta t}^{(i)}) (\boldsymbol{\psi}^{(j)}(\mathbf{X}_{\Delta t}^{(i)}))^T] + \mathbb{E}_{q_\phi(\boldsymbol{\tau})} [\text{diag}(\boldsymbol{\tau})] \quad (33)$$

$$\mathbf{S}_{\boldsymbol{\theta}_c}^{-1} \boldsymbol{\mu}_{\boldsymbol{\theta}_c} = \sigma_R^{-2} \sum_{i=1}^n \sum_{j=1}^{d_c} \mathbb{E}_{q_\phi(\mathbf{X}_{\Delta t}^{(i)})} [\boldsymbol{\psi}^{(j)}(\mathbf{X}_{\Delta t}^{(i)})] \quad (34)$$

The optimal posterior approximation for the hyperparameters $\boldsymbol{\tau} = \{\tau_m\}_{m=1}^M$ reduces to a product of independent Gamma-densities [56] with parameters γ_m and δ_m which are given by:

$$\gamma_m = \gamma_0 + 0.5, \quad \delta_m = \delta_0 + \frac{1}{2} (\boldsymbol{\mu}_{\boldsymbol{\theta}_c, m} + \mathbf{S}_{\boldsymbol{\theta}_c, (m, m)}) \quad (35)$$

Finally and since closed-form updates for the optimal posterior $q_\phi^{opt}(X_{\Delta t}^{(i)})$ are impossible, we employed Stochastic Variational Inference (SVI) as detailed in section 2.4 by assuming a multivariate lognormal (in order to ensure positivity

of $X_{\Delta t,j}$) with parameters $\phi = \{\boldsymbol{\mu}_i, \mathbf{S}_i\}_{i=1}^n$ ⁴. The gradients with respect to the parameters ϕ were estimated with Monte Carlo and the reparametrization trick [50] in order to reduce the variance of the estimates and ϕ were updated using stochastic gradient ascent (the ADAM algorithm of [57] in particular). The inference steps are summarized in Algorithm 3.

Algorithm 3: Inference algorithm for particle systems

Result: $\{q_\phi(\mathbf{X}_{\Delta t}^{(i)})\}_{i=1}^n, q(\boldsymbol{\theta}_c), q(\boldsymbol{\tau})$

Data: $\{\mathbf{X}_0^{(i)}, \hat{\mathbf{x}}_{\Delta t}^{(i)}\}_{i=1}^n$

- 1 Initialize the parameters for the variational distributions;
- 2 **while** *any of the parameters not converged* **do**
- 3 **for** $i \leftarrow 1$ **to** n **do**
- 4 | Update $q_\phi(\mathbf{X}_{\Delta t}^{(i)})$ by maximizing the ELBO (see Equation (28))
- 5 **end**
- 6 update $q(\boldsymbol{\theta}_c)$ according to Equation (33) and Equation (34) ;
- 7 update $q(\boldsymbol{\tau})$ according to Equation (35) ;
- 8 **end**

3.1.4. Advection-Diffusion system

For the simulations presented in this section $d_f = 250 \times 10^3$ particles were used, which, at each microscopic time step $\delta t = 2.5 \times 10^{-3}$ performed random, non-interacting, jumps of size $\delta s = \frac{1}{640}$, either to the left with probability $p_{left} = 0.1875$ or to the right with probability $p_{right} = 0.2125$. The positions were restricted in $[-1, 1]$ with periodic boundary conditions. It is well-known [58] that in the limit (i.e. $d_f \rightarrow \infty$) the particle density $\rho(s, t)$ can be modeled with an advection-diffusion PDE with diffusion constant $D = (p_{left} + p_{right}) \frac{\delta s^2}{2\delta t}$ and velocity $v = (p_{right} - p_{left}) \frac{\delta s}{\delta t}$:

$$\frac{\partial \rho}{\partial t} + v \frac{\partial \rho}{\partial s} = D \frac{\partial^2 \rho}{\partial s^2}, \quad s \in (-1, 1).. \quad (36)$$

For the CG description, 64 bins were employed i.e. $d_c = 64$ and a time step

⁴Diagonal covariances \mathbf{S}_i were employed

$\Delta t = 2$. Furthermore we employed first- and second-order feature function as in Equation (22) with a neighborhood size $H = 5$ which implies a total of $M = 77$ unknown parameters θ_c . We incorporate virtual observables pertaining to the residuals $\hat{\mathbf{R}}_0$ with $\sigma_R^2 = 10^{-6}$ (Equation (7))⁵ and the virtual observables $\hat{\mathbf{c}}_1$ pertaining to the conservation-of-mass constraint with $\sigma_c^2 = 10^{-10}$ (Equation (9)).

We employed $n = 32$ and $n = 64$ time sequences for training that were generated as detailed in section 3.1.3 with initial conditions $\{\mathbf{X}_0^{(i)}\}_{i=1}^n$ such as the ones seen in Figure 2. The initial conditions were generated by sampling the amplitude of a *sine* function, which was shifted up to ensure all values are positive and then normalized.

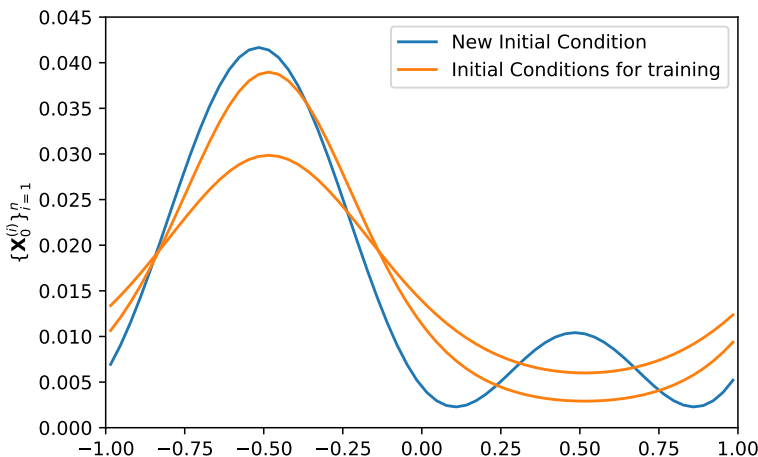


Figure 2: Sample initial conditions $\{\mathbf{X}_0^{(i)}\}_{i=1}^n$ for the Advection-Diffusion problem (orange) and an initial condition (blue) used for "extrapolative" predictions.

Figure 3 provides a histogram of the function values of the conservation-

⁵A very interesting possibility which is not explored here would be to learn σ_R^2 i.e. the strength of the enforcement of the CG evolution law from the data. This would increase the flexibility of the model in cases where the vocabulary of the feature functions selected in the right-hand side of the CG dynamics are not rich enough

of-mass constraint $\{c_1(\mathbf{X}_{\Delta t}^{(i)})\}_{i=1}^n$ upon convergence. The small values suggest that this has been softly incorporated in the CG states. A similar histogram for the residuals $R_{0,j}(\mathbf{X}^{(i)})_{i=1}^n$ is depicted in Figure 4 which also suggests enforcement of the CG evolution with the parameters $\boldsymbol{\theta}_c$ learned from the data $\boldsymbol{\theta}_c$. The evolution of the posterior mean $\boldsymbol{\mu}_{\boldsymbol{\theta}_c}$ (Equation (34)) of (a subset of) these parameters over the iterations of the SVI is depicted in Figure 5. Therein, and more clearly in Figure 6, one can observe the ability of the ARD prior to deactivate the vast majority of the right-hand-side feature functions and reveal a small subset of non-zero, salient terms. Both with $n = 32$ and $n = 64$ training data, only parameters $\boldsymbol{\theta}_c$ associated with first-order-interactions (Equation (22)) are activated. In particular, these are $\theta_{c,-3}^{(1)}$ and $\theta_{c,1}^{(1)}$ which are associated with the feature functions $X_{t,j-3}$ and $X_{t,j+1}$ respectively in Equation (22). This shares similarities with a finite-difference discretization scheme for the advection-diffusion and could be considered as an upwind scheme. The two identified coefficients do not form a centered difference operator but the center of the operator is shifted to the left and therefore takes into account the direction of the particle movement. As the value of the coefficients is not exactly the same the diffusive part is also captured.

Figure 7 depicts one of the inferred CG states $\mathbf{X}_{\Delta t}^{(i)}$ as well as the associated posterior uncertainty. Once the CG evolution law is learned, this state can be propagated into the future as detailed in section 2.5 in order to generate predictions. Indicative predictions (under "interpolative" conditions) can be seen in Figure 8 where the particle density up to $25\Delta t$ into the future is drawn. The latter as well as the associated uncertainty bounds are estimated directly from the reconstructed FG states. As one would expect, the predictive uncertainty grows, the further into the future one tries to predict. Figure 9 compares the predictive performance as a function of the training data used i.e. $n = 32$ or $n = 64$. In both cases, the ground truth is enveloped and as one would expect, more training data lead to smaller uncertainty bounds.

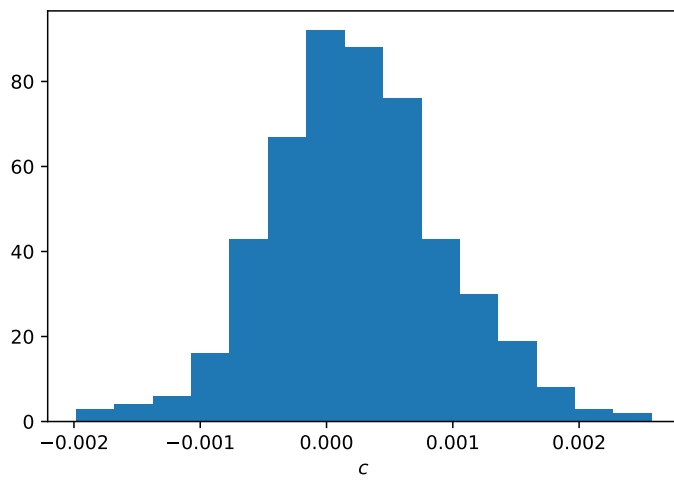


Figure 3: Error in the mass constraint

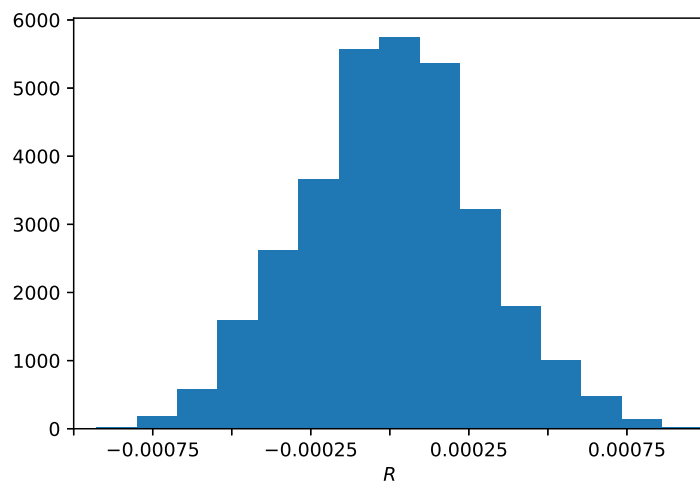


Figure 4: Error in the residual constraint

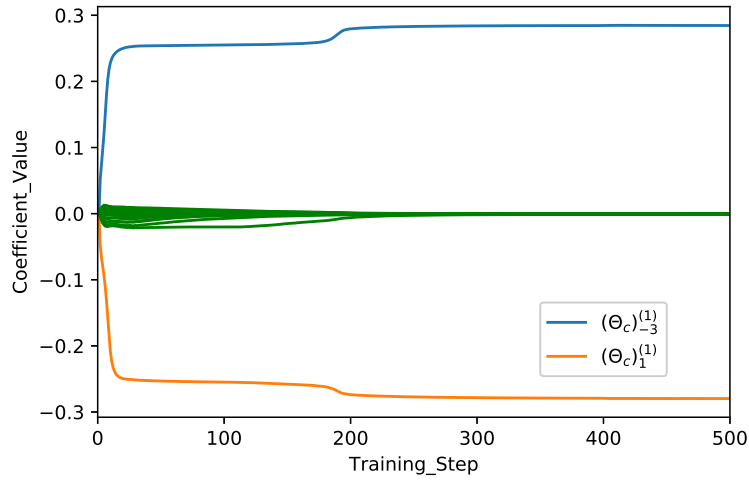


Figure 5: Evolution of a subset of θ_c parameters with respect to the iterations of the SVI for $n = 64$.

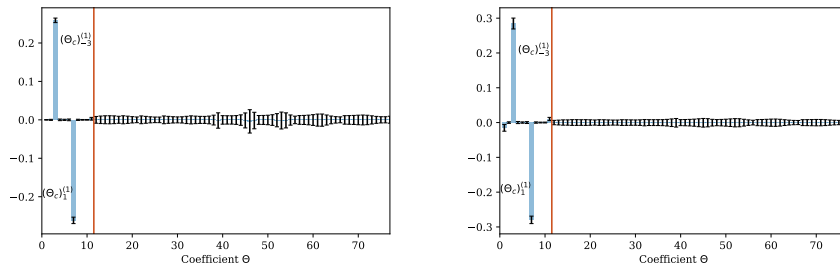


Figure 6: Comparison of the inferred parameters θ_c for $n = 32$ (left) and $n = 64$ (right) training data. The black bars indicate ± 1 standard deviation. The red vertical line separates first- from second-order coefficients.

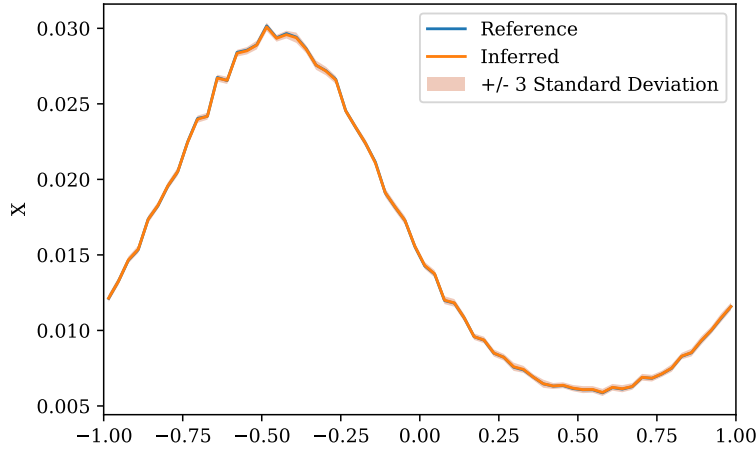


Figure 7: Inferred CG state $\mathbf{X}_{\Delta t}$ for one data sequence. Reference is obtained by sorting the particles into bins according to their position

We also tested the trained model (on $n = 64$) under "extrapolative" conditions i.e. for a different initial condition than the ones included in the training data (Figure 2). The predictive estimates in Figure 10 show very good agreement with the reference solution. It is important to point out that the model can correctly advect and diffuse the particle-bump initially introduced around $s = 0.5$ which suggests that the CG dynamics learned, reflect the most important features of the problem.

Finally, in Figure 11, the evolution of the mass constraint into the future is depicted and good agreement with the target value is observed.

3.1.5. Burgers' system

The second test-case involved an FG system of $d_f = 500 \times 10^3$ particles which perform *interactive* random walks i.e. the jump performed at each fine-scale time-step $\delta t = 2.5 \times 10^{-3}$ depends on the positions of the other walkers. In particular we adopted interactions as described in [59, 60, 53] so as, in the

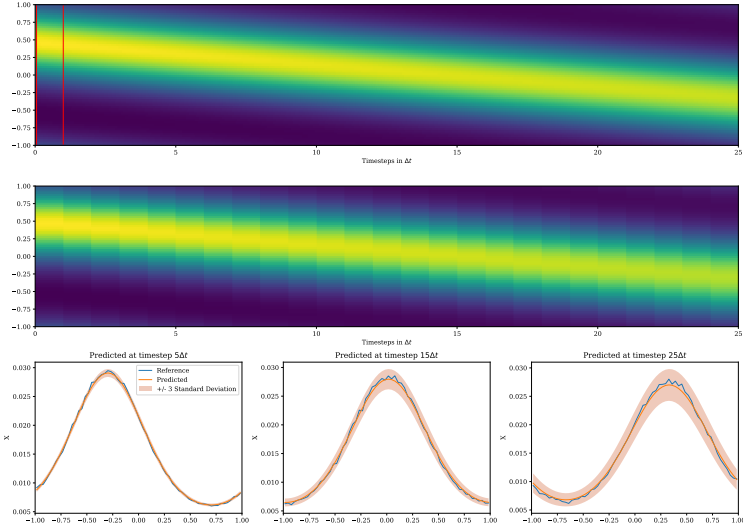


Figure 8: Prediction based on an initial condition contained in the training data. Top: Reference data (the vertical lines indicate the time instances with given data) , middle: Mean of the predictions, bottom: snapshots at three different time instances

limit (i.e. when $d_f \rightarrow \infty, \delta t \rightarrow 0, \delta s \rightarrow 0$), the particle density $\rho(s, t)$ follows the inviscid Burgers' equation:

$$\frac{\partial \rho}{\partial t} + \frac{1}{2} \frac{\partial \rho^2}{\partial s} = 0, \quad s \in (-1, 1). \quad (37)$$

For the CG description, 128 bins were employed i.e. $d_c = 128$ and a time step $\Delta t = 4$. As compared with the previous case, we enlarged the neighborhood size H in the first- and second-order interactions to $H = 8$, which yielded $M = 170$ right-hand-side terms in Equation (22). We incorporate virtual observables pertaining to the residuals $\hat{\mathbf{R}}_0$ with $\sigma_R^2 = 10^{-8}$ (Equation (7)) and the virtual observables $\hat{\mathbf{c}}_1$ pertaining to conservation-of-mass constraint with $\sigma_c^2 = 10^{-10}$ (Equation (9)).

We employed $n = 32$ and $n = 64$ time sequences for training that were

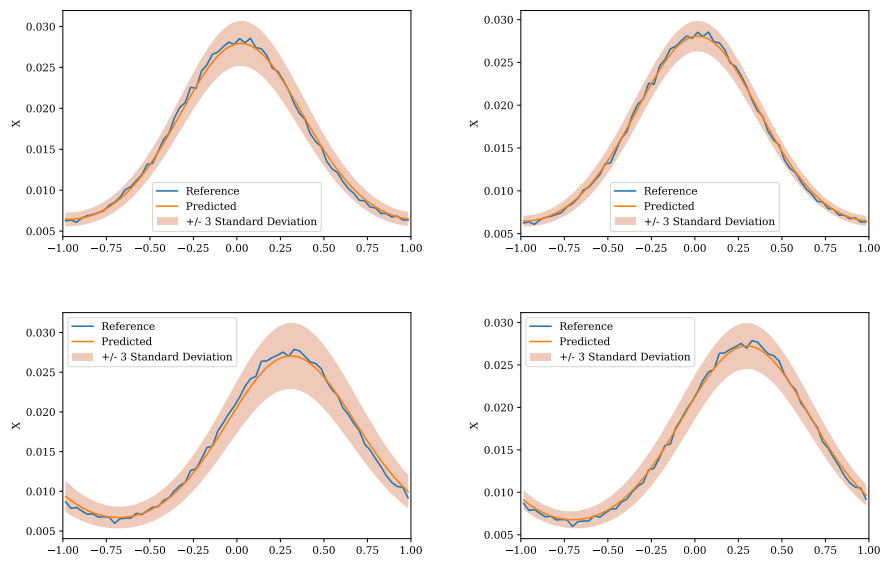


Figure 9: Comparison of the predictions for $n = 32$ (left) and $n = 64$ (right) at $15\Delta t$ (top) and $25\Delta t$ (bottom).

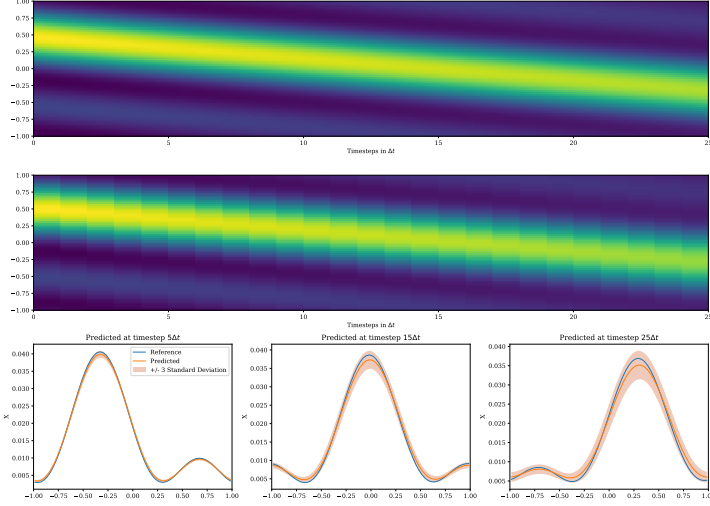


Figure 10: Prediction based on an initial condition NOT contained in the training data

generated as detailed in section 3.1.3 with initial conditions $\{\mathbf{X}_0^{(i)}\}_{i=1}^n$ such as the ones seen in Figure 12. They were generated by sampling the width and height of a triangular profile.

Figure 13 provides a histogram of the function values of the conservation-of-mass constraint $\{c_1(\mathbf{X}_{\Delta t}^{(i)})\}_{i=1}^n$ upon convergence. The small values suggest that this has been softly incorporated in the CG states. A similar histogram for the residuals $R_{0,j}(\mathbf{X}^{(i)})\}_{i=1}^n$ is depicted in Figure 14 which also suggests enforcement of the CG evolution with the parameters θ_c learned from the data θ_c . The evolution of the posterior mean μ_{θ_c} (Equation (34)) of (a subset of) these parameters over the iterations of the SVI is depicted in Figure 15. As in the previous example, in Figure 16 one can observe the ability of the ARD prior model to yield sparse solutions for the right-hand side of the CG evolution law. For all three training datasets with $n = 32, 64, 128$ time-sequences, only parameters θ_c associated with second-order-interactions (Equation (22)) are activated. In

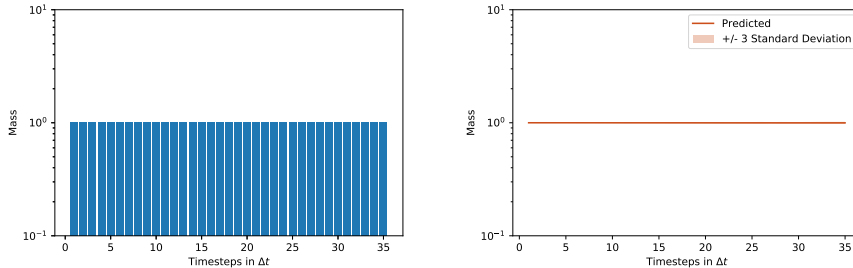


Figure 11: Evolution of the mass constraint during predictions

particular, these are the negative coefficient $\theta_{c,(0,0)}^{(2)}$ (in all three cases) as well as different second-order coefficients. In the cases of $n = 32$ and $n = 64$ two coefficients are found with positive mean and high posterior uncertainty, but they also have negative posterior correlation (correlation coefficient of -0.88). As all activated coefficients pertain to feature-functions involving the actual bin or bins to the left, the learned evolution law could be interpreted as an up-wind scheme, which takes the direction of the Burgers' flow into account. Such schemes are considered advantageous in for numerical simulations of fluid flows.

Figure 17 depicts one of the inferred CG states $\mathbf{X}_{\Delta t}^{(i)}$ as well as the associated posterior uncertainty. Given the learned CG dynamics, this state can be propagated into the future as detailed in section 2.5 in order to generate predictions. Indicative predictions (under "interpolative" conditions) can be seen in Figure 18 where the particle density up to $25\Delta t$ into the future is drawn. The latter as well as the associated uncertainty bounds are estimated directly from the reconstructed FG states. As in the previous example, the predictive uncertainty grows, the further into the future one tries to predict. Figure 19 compares the predictive performance as a function of the training data used i.e. $n = 32$ or $n = 64$. The increase in data leads for this example to a better fit of the posterior mean to the reference, which captures the location of the shock more precisely. The predictive uncertainty bounds are particularly large at the location of the shock which is the most challenging component in such systems.

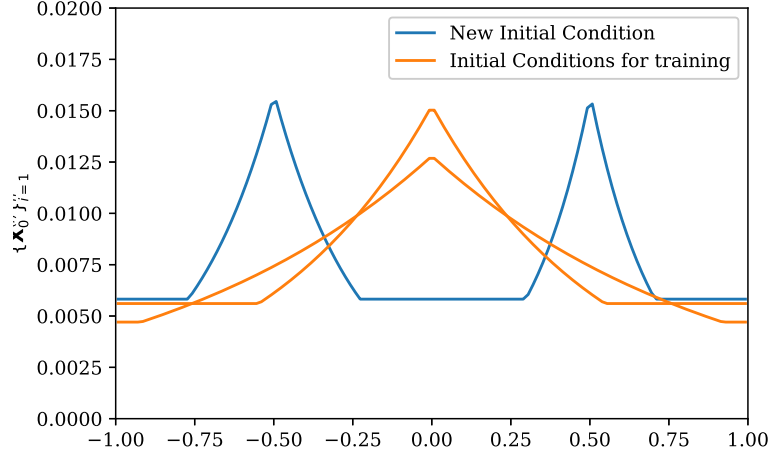


Figure 12: Sample initial conditions $\{\mathbf{X}_0^{(i)}\}_{i=1}^n$ for the Burgers' problem (orange) and an initial condition (blue) used for "extrapolative" predictions.

We also test the trained model (on $n = 64$) under "extrapolative" conditions i.e. for a different with a "bimodal" initial condition which was quite different than the ones included in the training data (Figure 12). The predictive estimates in Figure 20 show very good agreement with the reference solution. We want to point out that the trained model is capable of capturing the development, the position as well as the propagation of a shock front.

Finally, in Figure 21, the evolution of the mass constraint into the future is depicted and good agreement with the target value is observed.

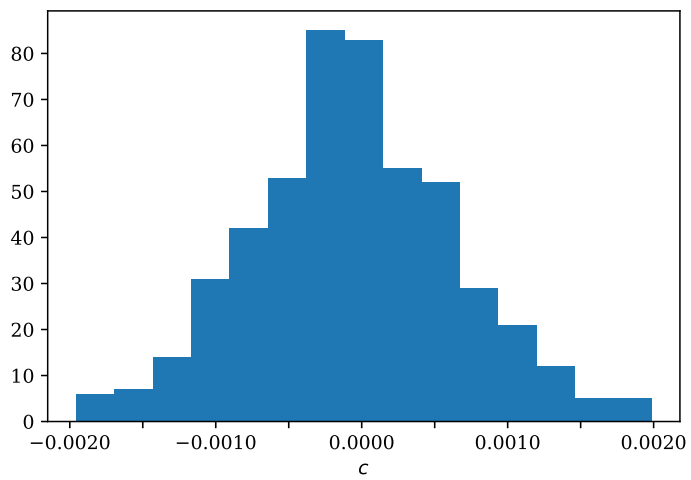


Figure 13: Error in the mass constraint

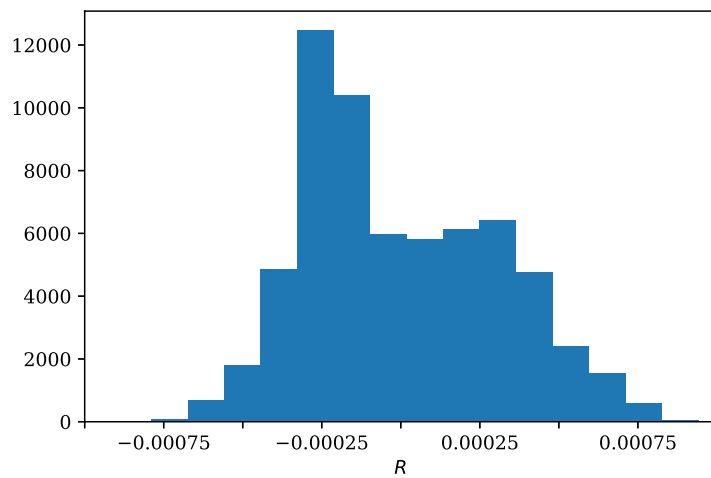


Figure 14: Error in the residual constraint

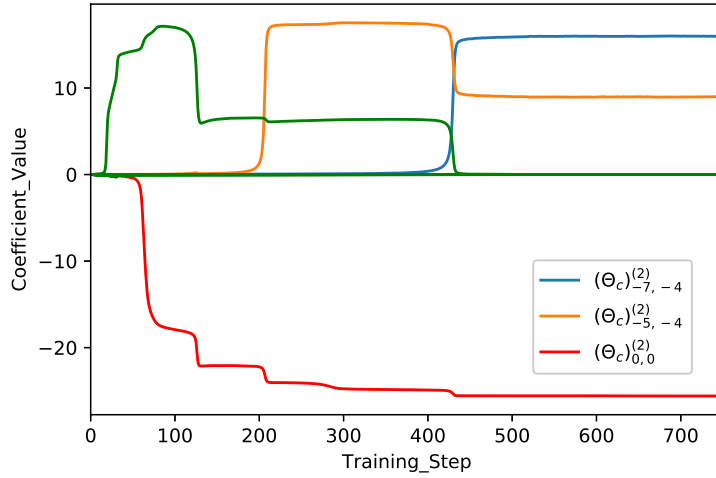


Figure 15: Evolution of a subset of θ_c parameters with respect to the iterations of the SVI for $n = 64$.

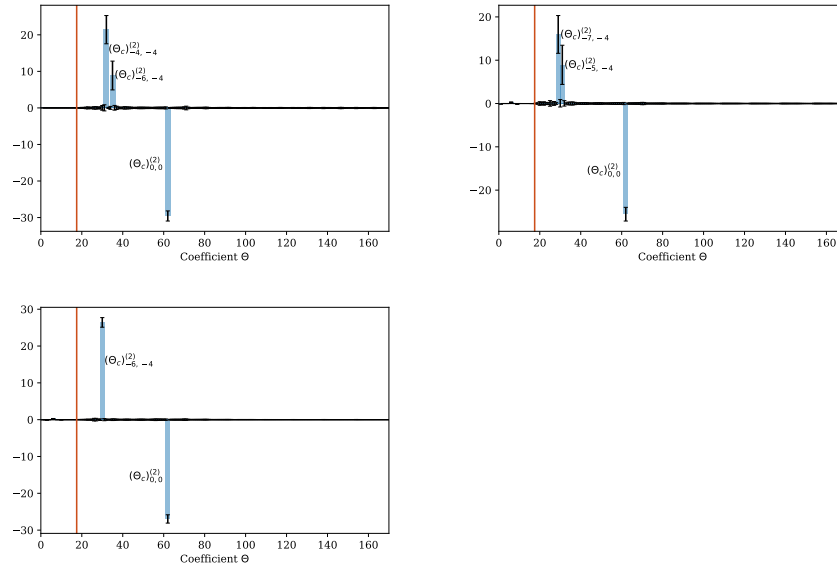


Figure 16: Comparison of the inferred parameters θ_c for $n = 32$ (top-left), $n = 64$ (top-right) and $n = 128$ (bottom-left) training data. The black bars indicate ± 1 standard deviation. The red vertical line separates first- from second-order coefficients.

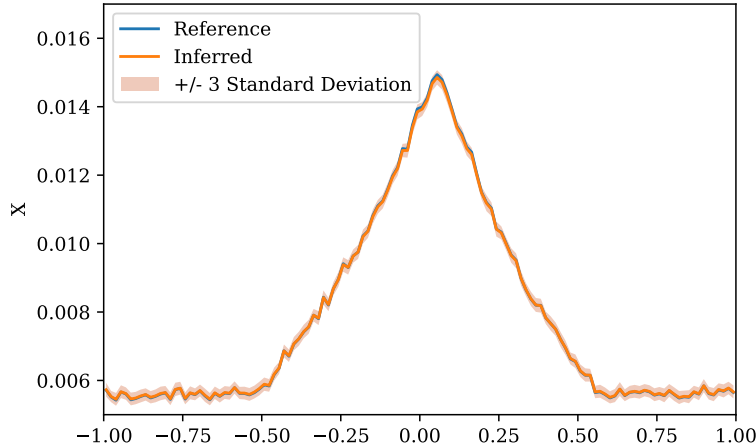


Figure 17: Example of inferred CG state $\mathbf{X}_{\Delta t}^{(i)}$ for data sequence i .

3.2. Nonlinear Pendulum

In this final example we consider time sequences of images of a nonlinear pendulum in two dimensions as in [21]. For the FG data we generate a series of black-and-white images of a moving disc tied on a string and forming a pendulum (see Figure 31). The images consisted of 29×29 pixels each and each pixel's value was either 1 (occupied) or -1 (unoccupied). Hence \mathbf{x}_t was a $d_f = 29^2 = 581$ -dimensional vector of binary variables. The dynamics of the pendulum can be fully described by the rotation angle y_t which follows a nonlinear, second-order ODE of the form:

$$\ddot{y}_t + \sin(y_t) = 0 \tag{38}$$

The primary goal is to identify the right CG variables as well as CG dynamics solely from image data i.e. binary vectors $\{\hat{\mathbf{x}}_{0:T\Delta t}^{(i)}\}^{1:n}$ collected over T time-steps as the pendulum is initialized from n states/positions. The length of time sequences in the following numerical results was $T = 74$ and the CG time-step

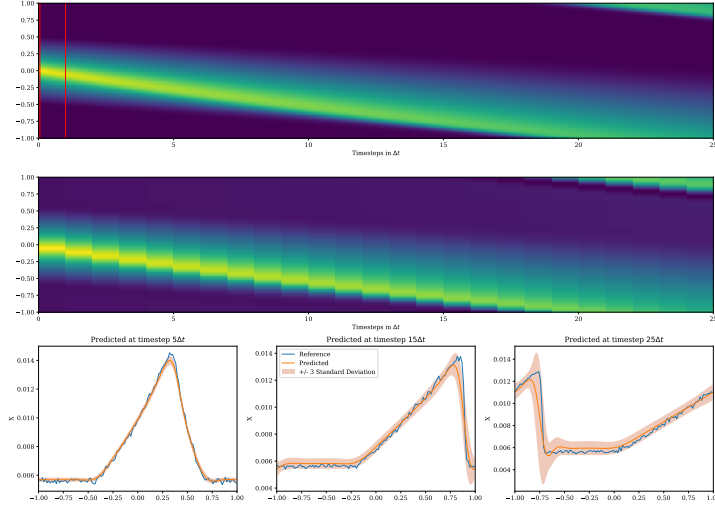


Figure 18: Prediction based on an initial condition contained in the training data. Top: Reference data (the vertical lines indicate the time instances with given data), middle: Mean of the predictions, bottom: snapshots at three different time instances

$$\Delta t = 0.05^6.$$

3.2.1. CG variables and coarse-to-fine mapping

The only knowledge introduced a priori with regards to the CG variables \mathbf{X}_t is that $\dim(\mathbf{X}) = d_c = 2$. We intend to investigate procedures that can automatically identify d_c i.e. the number of CG variables. We note at this stage that such efforts should be guided by the ELBO \mathcal{F} (e.g. Equation (19)) which approximates the model evidence and therefore provides a natural Bayesian score for comparing models with different numbers of CG variables.

The other pertinent model component is the coarse-to-fine map which is enabled by the $p_{cf}(\mathbf{x}_t|\mathbf{X}_t)$ (section 2.3). To that end, we employed the following

⁶For the generation of images a *microscopic* time-step $\delta t = 0.01$ for the integration of Equation (38) was used.

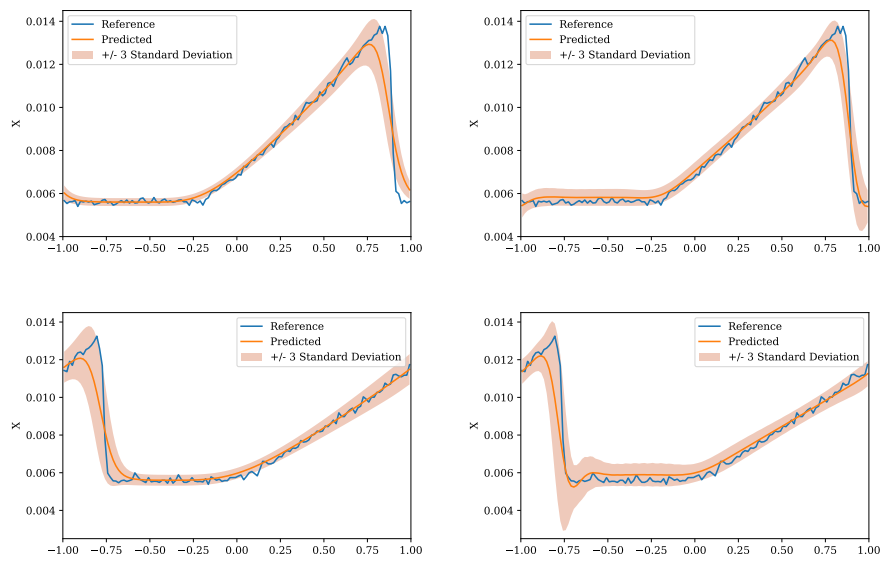


Figure 19: Comparison of the predictions for $n = 32$ (left) and $n = 64$ (right) training data at $15\Delta t$ (top) and $25\Delta t$ (bottom).

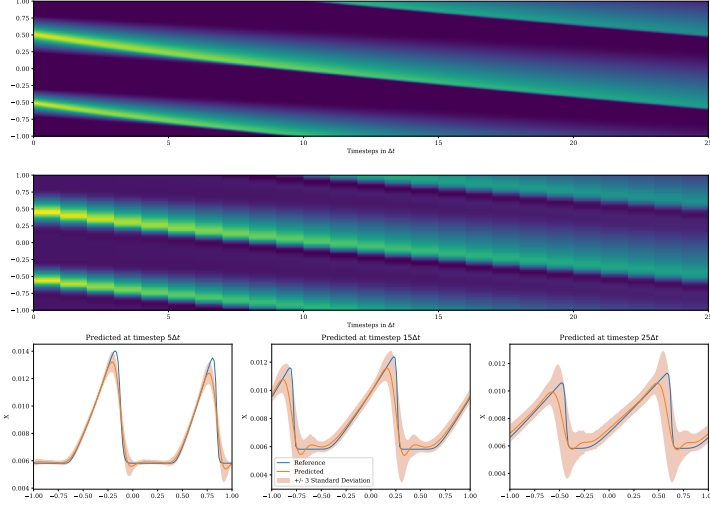


Figure 20: Prediction based on an initial condition NOT contained in the training data. Top: Reference data , middle: Mean of the predictions, bottom: snapshots at three different time instances

logistic model⁷:

$$p_{cf}(\mathbf{x}|\mathbf{X}) = \prod_{s=1}^{d_f} \frac{1}{1 + \exp(-x_s G_s(\mathbf{X}; \boldsymbol{\theta}_{cf}))} \quad (39)$$

where x_s is the value (± 1) of each of the pixels $s = 1, \dots, d_f$. For the link functions $\{G_s\}_{s=1}^{d_f}$, we employed a deep neural net with weights $\boldsymbol{\theta}_{cf}$, the details of which are shown in Figure 22. One fully connected layer followed by two transposed convolutional layers were found to be flexible enough to accurately represent the functions G_s . The CNNs were specifically chosen because of their ability to extract/map features from/to images.

⁷we omit the time-index t for clarity

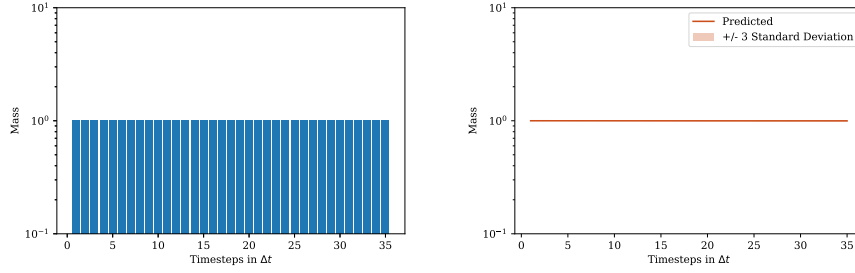


Figure 21: Evolution of the mass during predictions

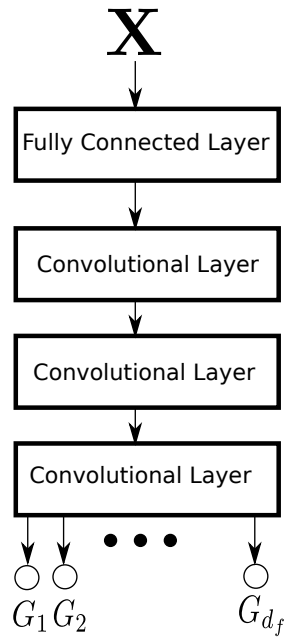


Figure 22: Deep neural net employed for the link functions G_s (Equation (39)). After one dense layer which $32 \cdot 7 \cdot 7$ nodes and rectified linear unit activation function (ReLU), two two-dimensional transposed convolutional layers with 32 filters and a kernel size of 3 as well as a ReLU activation function are applied followed by one-last two-dimensional transposed convolutional layers with one filter, kernel size 3 and without activation to generate the functions G_s .

3.2.2. The CG evolution law and the virtual observables

With regards to the evolution law of the CG states $\mathbf{X}_t = \{X_{t,1}, X_{t,2}\}$, we postulate the following form:

$$\begin{aligned}\dot{X}_{t,1} &= F_1(\mathbf{X}_t, \boldsymbol{\theta}_c) = X_{t,2} \\ \dot{X}_{t,2} &= F_2(\mathbf{X}_t, \boldsymbol{\theta}_c) = \boldsymbol{\theta}_c^T \boldsymbol{\psi}(X_{t,1}) = \sum_{m=0}^M \theta_{c,m} \psi_m(X_{t,1})\end{aligned}\quad (40)$$

where $\boldsymbol{\theta}_c$ denote the associated parameters. In total we employed $M = 101$ feature functions of the following type:

$$\psi_m(X) = \begin{cases} 1, & m = 0 \\ \cos(mX), & m = 1, \dots, M/2 = 50 \\ \sin((m - 50)X), & m = 51, \dots, M = 100 \end{cases}\quad (41)$$

The form of Equation (40) implies a second-order ODE where the second CG variable plays the role of the velocity. With regards to the parameters $\boldsymbol{\theta}_c$, the sparsity-inducing ARD prior detailed in section 3.1.2 was employed.

To enforce the associated dynamics, we made use of the symplectic Euler time-discretization scheme, which is a first-order integrator, that is explicit in one coordinate ($X_{t,1}$) and *implicit* in the other ($X_{t,2}$)⁸. The associated virtual observables (see Equation (6)) were enforced with $\sigma_R^2 = 10^{-5}$.

3.2.3. Inference and Learning

As in the previous examples (Equation (27)), the approximate posterior was factorized as:

$$q_\phi(\mathbf{X}_{0:T\Delta t}^{(1:n)}, \boldsymbol{\theta}_c, \boldsymbol{\tau}) = \prod_{i=1}^n q_\phi(\mathbf{X}_{0:T\Delta t}^{(i)}) q(\boldsymbol{\theta}_c) q(\boldsymbol{\tau})\quad (42)$$

and closed-form updates were used for $q(\boldsymbol{\theta}_c)$ (see Equations (33) and (34)) and $q(\boldsymbol{\tau})$ (see Equation (35)).

⁸This corresponds to a multistep method in Equation (4) with $K = 1$, $a_0 = 1, a_1 = -1, \beta_0 = 0, \beta_1 = -1$ for the explicit part and $K = 1$, $a_0 = 1, a_1 = -1, \beta_0 = -1, \beta_1 = 0$ for the implicit part

SVI is applied for the posteriors densities $q_\phi(\mathbf{X}_{0:T \Delta t}^{(i)})$ on the vector of the latent CG states $\mathbf{X}_{0:T \Delta t}^{(i)}$ which we approximated with multivariate Gaussians. Since the posterior reveal the fine-to-coarse map which apart from insight can be used for predictive purposes as well, we employed an *amortized* version of SVI ([50]) i.e. explicitly accounted for the dependence of each $q_\phi(\mathbf{X}_{0:T \Delta t}^{(i)})$ on the corresponding FG observables $\hat{\mathbf{x}}_{0:T \Delta t}^{(i)}$ i.e.:

$$q_\phi(\mathbf{X}_{0:T \Delta t}^{(i)}) = \mathcal{N}(\boldsymbol{\mu}_\phi(\hat{\mathbf{x}}_{0:T \Delta t}^{(i)}), \mathbf{S}_\phi(\hat{\mathbf{x}}_{0:T \Delta t}^{(i)})) \quad (43)$$

The parameters ϕ were the weights of a deep convolutional neural net, the architecture of which is shown in Figure 23. This was chosen because it mirrors the DNN architecture employed for the coarse-to-fine map in Figure 22.

Finally it should be mentioned that the "slowness" prior was employed on the hidden states $\mathbf{X}_{0:T \Delta t}^{(1:n)}$ as described in Equation (16)⁹. Maximum-likelihood estimates for the hyperparameter $\sigma_{\mathbf{X}}^2$ were employed which readily arise by differentiating the ELBO \mathcal{F} and which yield the following update equation:

$$\sigma_{\mathbf{X}}^2 = \frac{1}{n T d_c} \sum_{i=1}^n \sum_{l=0}^{T-1} \mathbb{E}_{q_\phi(\mathbf{X}_{0:T \Delta t}^{(i)})} \left[\left| \mathbf{X}_{(l+1) \Delta t}^{(i)} - \mathbf{X}_{l \Delta t}^{(i)} \right|^2 \right] \quad (44)$$

Maximum likelihood estimates were also obtained for the parameters $\boldsymbol{\theta}_{cf}$ (Equation (39)) by numerically differentiating the ELBO \mathcal{F} and performing Stochastic Gradient Ascent (SGA).

A general summary of the steps involved for the inference procedure is can be found in Algorithm 4. For the implementation we made use of the Tensorflow framework [61].

⁹For the prior distribution $p_{c,0}(\mathbf{X}_0^{(i)})$ a Gaussian mixture distribution with means +1.5 and -1.5 and standard deviation 1.5 was used.

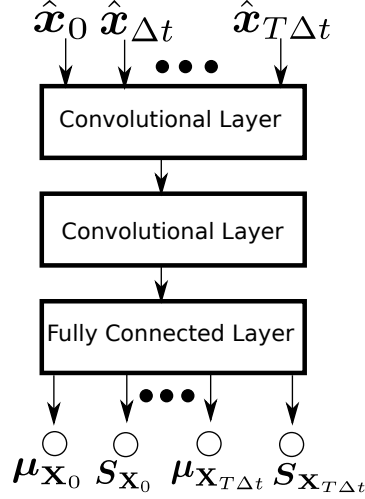


Figure 23: The input consists of a time series of pictures of the pendulum and can therefore be considered to be three-dimensional, where the first and second dimension are the number of pixels and the third dimension is the number of time steps available for training. This input is given to a three-dimensional convolutional layer with kernel size $(3, 3, 2)$, 32 filters and a ReLU activation followed by another three-dimensional convolutional layer with kernel size 2 in each dimension, 64 filters and a ReLU activation. The last layer is a fully connected layer with $2d_c \cdot T$ nodes and without activation to generate the mean and variance values for each time step of the inferred \mathbf{X} coordinates.

Algorithm 4: Algorithm for the Pendulum system

Result: $\phi, q(\theta_c), q(\tau), \theta_{cf}, \sigma_{\mathbf{X}}$

Data: $\hat{\mathbf{x}}_{0:T\Delta t}^{(1:n)}$

- 1 Initialize all required parameters;
 - 2 **while** *ELBO not converged* **do**
 - 3 Update the parameters θ_{cf} and ϕ by SGA of the ELBO (Equation (19)) ;
 - 4 update $q(\theta_c)$ according to Equation (33) and Equation (34) ;
 - 5 update $q(\tau)$ according to Equation (35) ;
 - 6 update the parameter $\sigma_{\mathbf{X}}$ according to Equation (44)
 - 7 **end**
-

3.2.4. Results

Each data sequence $\hat{\mathbf{x}}_{0:T\Delta t}^{(i)}$ used consisted of 75 images i.e. $T = 74$ generated with a time-step $\Delta t = 0.05$ (Figure 24). We investigated two cases for the number of data sequences i.e. $n = 16$ and $n = 64$. The data generation involved sampling uniformly the $y_0 \in [-\pi, \pi]$ and assuming zero initial velocity i.e. $\dot{y}_0 = 0$. None of data series consisted of a complete oscillation.

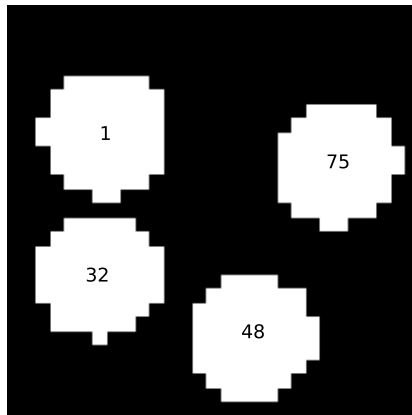


Figure 24: Sample data sequence $\hat{\mathbf{x}}_{0:T\Delta t}^{(i)}$ for the nonlinear pendulum problem. The number indicates the corresponding time-step.

Figure 25 indicates the posterior means of the inferred θ_c that parametrize the CG evolution law (Equation (40)) for $n = 16$ and $n = 64$. Of the 101 possible terms, only 2 are activated due the ARD prior.

Figure 26 illustrates trajectories in the two-dimensional CG state-space obtained with various initial conditions for the CG model identified with $n = 16$ and $n = 64$ data sequences. The blue curves correspond to "interpolative" settings i.e. to the CG states of an observed sequence of images, whereas the orange curves to "extrapolative settings" i.e. to the CG states inferred by initializing the pendulum from an arbitrary position *not* contained in the training data. In Figure 27 the predicted evolution in time of both coarse-grained variables is

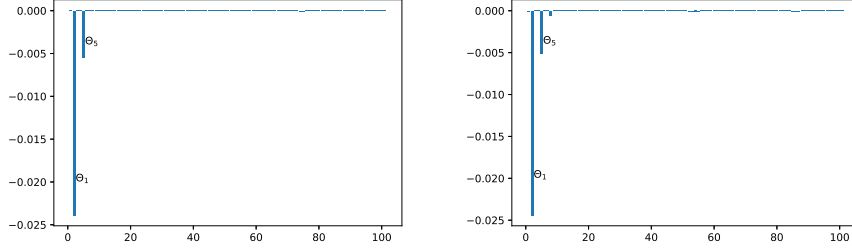


Figure 25: Posterior means of the inferred θ_c that parametrize the CG evolution law (Equation (40)) for $n = 16$ (left) and $n = 64$ (right).

shown. The periodic nature of the CG dynamics is obvious, even though the CG state variables implicitly identified do not correspond to the natural ones i.e. y_t and \dot{y}_t .

This can be seen in Figure 28 where for data-sequences $\mathbf{x}_{0:T\Delta t}^{(i)}$ (corresponding to the pendulum at various positions i.e. angles $y_{0:T\Delta t}$), we compute from the approximate posterior $q_\phi(\mathbf{X}_{0:T\Delta t}^{(i)}|\mathbf{x}_{0:T\Delta t}^{(i)})$ (Equation (43)) the mean of the corresponding CG states $\mathbf{X}_{0:T\Delta t}^{(i)}$ as well as the (in this case negligible) standard deviation. For each time instant $l = 0, 1, \dots, T$, we plot the pairs of $y_{l\Delta}$ and (the mean of) $X_{l\Delta,1}$ (i.e. the first of the CG variables identified) to show the relation between the two variables. While it is obvious from the scales that the first CG variable identified is *not* the angle, it appears to be isomorphic to y . The latter property persists for $n = 64$ even though the sign of the relation has been reversed. The difference between the first CG variable identified and the natural angle y explains the difference between the CG evolution law identified (Figure 25) and the reference one Equation (38).

Figure 29 provides predictive estimates of the position of the center of mass in time. These were obtained by propagating the CG variables in time and for each time instant, sampling p_{cf} for corresponding images \mathbf{x} . From the latter, the center of mass was computed from the activated pixels i.e. the pixels with value 1. Naturally, predictive uncertainty arises due the stochasticity in the initial conditions of \mathbf{X} as well as in p_{cf} . The latter is quantified by the standard

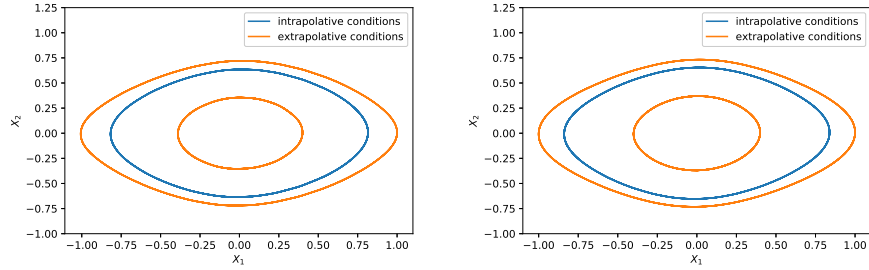


Figure 26: Comparison of trajectories for $n = 16$ (left) training data and $n = 64$ (right) training data.

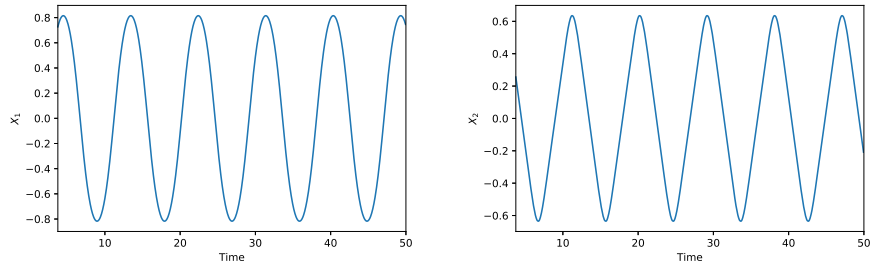


Figure 27: Predicted posterior mean of the dynamics of the coarse-grained coordinates

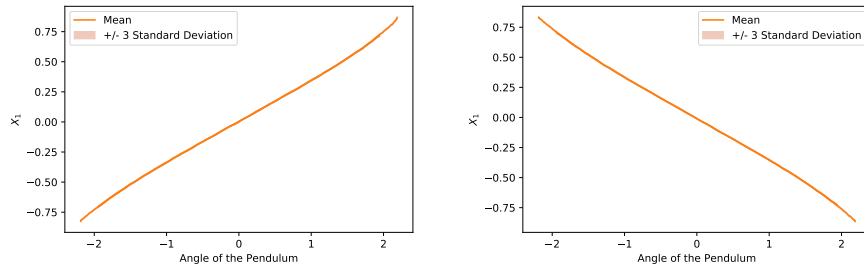


Figure 28: Mapping between the angle of the pendulum and the coarse-grained coordinates for 32 training data and 64 (right) training data.

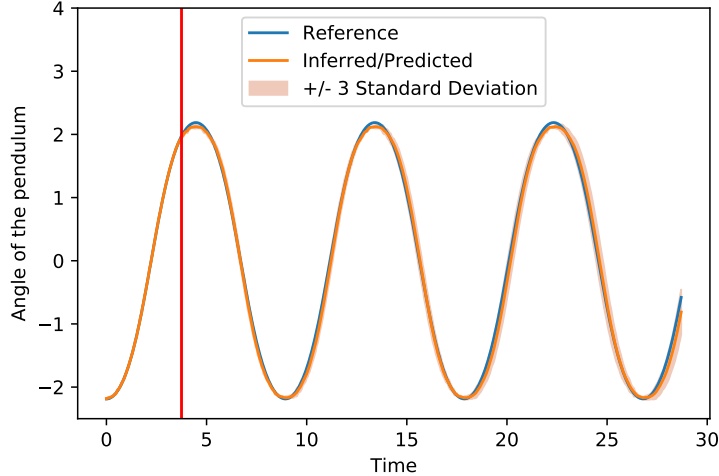


Figure 29: Inferred/Predicted evolution of the center of mass of the pendulum. The vertical line separates the inferred states from the predictions

deviation and plotted in Figure 29. As in the previous examples, the predictive uncertainty grows, albeit modestly, with time.

Figure 30 depicts predictions in time for two pixels in the image. One can clearly distinguish the changepoints i.e. when the pendulum crosses the pixel and its value is changed from 0 to 1 as well as the predictive uncertainty which is concentrated at those changepoints. This demonstrates one of the strengths of our approach as due to the coarse-to-fine mapping the whole FG state is reconstructed and every observable can be computed together with the respective uncertainty.

Finally Figure 31 compares actual images obtained by the reference dynamics of the pendulum with the predictive posterior mean obtained by the CG model and p_{cf} trained on the data. Even though these extend up to 875 time-steps i.e. more than 11 times longer than the time-window over which observations were available, they match the reference quite accurately, a strong indication that the right CG variables and CG dynamics have been identified. An animation containing all frames can be found by following this [link](#).

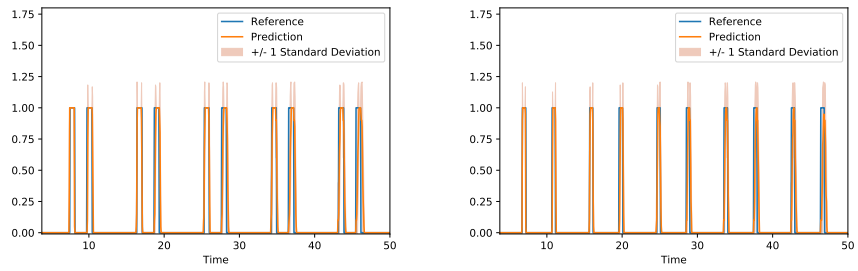
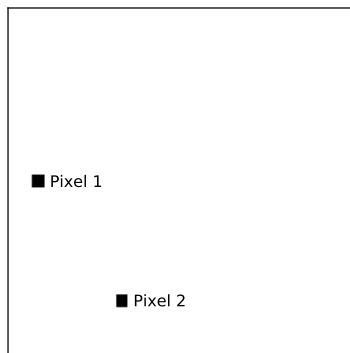


Figure 30: Predicted time history of a single pixel: Pixel 1 (left) and Pixel 2 (right)

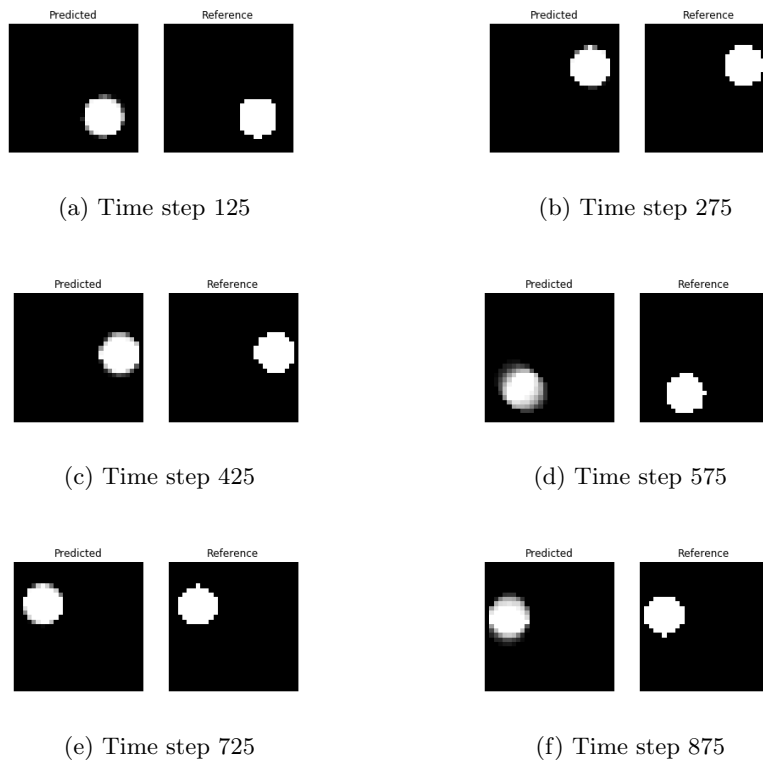


Figure 31: Predictive posterior means of images of the pendulum compared to the reference data

4. Conclusions

We proposed a probabilistic generative model for the automated discovery of CG descriptions and CG dynamics based on FG simulation data. The target density is augmented in a fully Bayesian fashion by virtual observables that enable the incorporation of physical constraints that appear in the form of equalities. This could involve residuals of the CG evolution law or more importantly conservation laws that are available when CG variables have physical meaning. This is particularly important in the context of physical modeling as in many cases such domain knowledge is a priori available and its integration can, not only reduce the amount of training data, but endow the CG model learned with the necessary features that would allow it to provide accurate predictions in out-of-distribution settings. Our approach learns simultaneously a coarse-to-fine mapping and an evolution law for the coarse-grained dynamics by employing probabilistic inference tools for the latent variables and model parameters. The use of deep neural nets for the former component can endow great expressiveness and flexibility. The concept of sparsity, which is invoked in learning CG dynamics from a large vocabulary of right-hand-side terms, is readily incorporated using sparsity-inducing Bayesian priors without any hyperparameter tuning. As a result of the aforementioned characteristics, the framework can learn from *Small Data* which is a crucial advantage in multi-scale models where the simulation of the FG dynamics is expensive and slow in exploring the state-space. The model proposed was successfully tested on coarse-graining tasks from different areas. In all three examples, the method performed well under interpolative, and more importantly under extrapolative settings i.e. in cases where initial conditions different from the ones seen during training, are prescribed. Moreover, as it is able to reconstruct the entire FG state vector at any future time instant, it is capable of producing predictions of any FG observable of interest as well as quantify the associated predictive uncertainty.

There exists various possibilities to extend the proposed framework, both

methodologically as well as applications are concerned. In the latter case and apart from using it for predictive purposes, the CG model learned could also be employed in optimization and control applications. On the methodological front an obvious extension would be to account for the virtual observables at future time-instants as well. This would ensure their enforcement by future CG states but would unavoidably complicate their simulation as a probabilistic inference scheme would need to be employed in order to draw samples.

References

- [1] D. Givon, R. Kupferman, A. Stuart, Extracting Macroscopic Dynamics: Model Problems and Algorithms, Nonlinearity.
- [2] W. Bialek, Biophysics: Searching for Principles, Princeton University Press, 2012.
- [3] Z. Ghahramani, Probabilistic machine learning and artificial intelligence, Nature 521 (7553) (2015) 452–459. doi:10.1038/nature14541.
URL <http://www.nature.com/nature/journal/v521/n7553/full/nature14541.html>
- [4] Y. LeCun, Y. Bengio, G. Hinton, Deep learning, nature 521 (7553) (2015) 436–444.
- [5] P.-S. Koutsourelakis, N. Zabaras, M. Girolami, Big data and predictive computational modeling, Journal of Computational Physics 321 (2016) 1252–1254.
- [6] G. Marcus, E. Davis, Rebooting AI: Building Artificial Intelligence We Can Trust, Pantheon, 2019.
- [7] P. Stinis, T. Hagge, A. M. Tartakovsky, E. Yeung, Enforcing constraints for interpolation and extrapolation in generative adversarial networks, Journal of Computational Physics 397 (2019) 108844.
- [8] P.-S. Koutsourelakis, E. Bilonis, Scalable Bayesian Reduced-Order Models for Simulating High-Dimensional Multiscale Dynamical Systems, Multiscale Modeling & Simulation 9 (1) (2011) 449–485. doi:10.1137/100783790.
- [9] P. J. Schmid, Dynamic mode decomposition of numerical and experimental data, Journal of Fluid Mechanics 656 (2010) 5–28. doi:10.1017/S0022112010001217.
URL <https://www.cambridge.org/core/>

journals/journal-of-fluid-mechanics/article/
dynamic-mode-decomposition-of-numerical-and-experimental-data/
AA4C763B525515AD4521A6CC5E10DBD4

- [10] M. O. Williams, I. G. Kevrekidis, C. W. Rowley, A DataDriven Approximation of the Koopman Operator: Extending Dynamic Mode Decomposition, *Journal of Nonlinear Science* 25 (2015) 1307–1346. doi:10.1007/s00332-015-9258-5.
- [11] H. Wu, F. Noé, Variational approach for learning Markov processes from time series data, arXiv:1707.04659 [math, stat].
URL <http://arxiv.org/abs/1707.04659>
- [12] G. Froyland, G. A. Gottwald, A. Hammerlindl, A Computational Method to Extract Macroscopic Variables and Their Dynamics in Multiscale Systems, *SIAM Journal on Applied Dynamical Systems* 13 (4) (2014) 1816–1846. doi:10.1137/130943637.
URL <https://epubs.siam.org/doi/abs/10.1137/130943637>
- [13] L. Felsberger, P. Koutsourelakis, Physics-constrained, data-driven discovery of coarse-grained dynamics, *Communications in Computational Physics* 25 (5) (2019) 1259–1301. doi:10.4208/cicp.0A-2018-0174.
- [14] A. Mardt, L. Pasquali, H. Wu, F. Noé, VAMPnets for deep learning of molecular kinetics, *Nature Communications* 9. doi:10.1038/s41467-017-02388-1.
URL <https://www.ncbi.nlm.nih.gov/pmc/articles/PMC5750224/>
- [15] H. Wu, A. Mardt, L. Pasquali, F. Noe, Deep generative markov state models, in: *Advances in Neural Information Processing Systems*, 2018, pp. 3975–3984.
- [16] L. Duncker, G. Böhner, J. Boussard, M. Sahani, Learning interpretable continuous-time models of latent stochastic dynamical systems, arXiv preprint arXiv:1902.04420.

- [17] C. Grigo, P.-S. Koutsourelakis, A physics-aware, probabilistic machine learning framework for coarse-graining high-dimensional systems in the small data regime, arXiv preprint arXiv:1902.03968.
- [18] Y. Pantazis, I. Tsamardinos, A unified approach for sparse dynamical system inference from temporal measurements, *Bioinformatics* 35 (18) (2019) 3387–3396. doi:10.1093/bioinformatics/btz065.
URL <https://academic.oup.com/bioinformatics/article/35/18/3387/5305020>
- [19] S. L. Brunton, J. L. Proctor, J. N. Kutz, Discovering governing equations from data by sparse identification of nonlinear dynamical systems, *Proceedings of the National Academy of Sciences* 113 (15) (2016) 3932–3937.
- [20] E. Kaiser, J. N. Kutz, S. L. Brunton, Sparse identification of nonlinear dynamics for model predictive control in the low-data limit, *Proceedings of the Royal Society A* 474 (2219) (2018) 20180335.
- [21] K. Champion, B. Lusch, J. N. Kutz, S. L. Brunton, Data-driven discovery of coordinates and governing equations, arXiv preprint arXiv:1904.02107.
- [22] J. Ohkubo, Nonparametric model reconstruction for stochastic differential equations from discretely observed time-series data, *Physical Review E* 84 (6) (2011) 066702. doi:10.1103/PhysRevE.84.066702.
URL <https://link.aps.org/doi/10.1103/PhysRevE.84.066702>
- [23] S. Klus, F. Nske, P. Koltai, H. Wu, I. Kevrekidis, C. Schtte, F. No, Data-Driven Model Reduction and Transfer Operator Approximation, *Journal of Nonlinear Science* 28 (3) (2018) 985–1010. doi:10.1007/s00332-017-9437-7.
URL <https://doi.org/10.1007/s00332-017-9437-7>
- [24] B. O. Koopman, Hamiltonian Systems and Transformations in Hilbert Space, *Proceedings of the National Academy of Sciences of the United*

States of America 17 (5) (1931) 315–318.

URL <https://www.jstor.org/stable/86114>

- [25] I. Mezić, Spectral properties of dynamical systems, model reduction and decompositions, *Nonlinear Dynamics* 41 (1-3) (2005) 309–325.
- [26] S. L. Brunton, B. W. Brunton, J. L. Proctor, J. N. Kutz, Koopman invariant subspaces and finite linear representations of nonlinear dynamical systems for control, *PloS one* 11 (2) (2016) e0150171.
- [27] M. A. Katsoulakis, P. Plecháč, Information-theoretic tools for parametrized coarse-graining of non-equilibrium extended systems, *The Journal of chemical physics* 139 (7) (2013) 074115.
- [28] V. Harmandaris, E. Kalligiannaki, M. Katsoulakis, P. Plech, Path-space variational inference for non-equilibrium coarse-grained systems, *Journal of Computational Physics* 314 (2016) 355–383. doi:10.1016/j.jcp.2016.03.021.
URL <http://www.sciencedirect.com/science/article/pii/S002199911600173X>
- [29] M. A. Katsoulakis, P. Vilanova, Data-driven, variational model reduction of high-dimensional reaction networks, *Journal of Computational Physics* (2019) 108997.
- [30] H. Mori, Transport, collective motion, and brownian motion, *Progress of theoretical physics* 33 (3) (1965) 423–455.
- [31] R. Zwanzig, Nonlinear generalized langevin equations, *Journal of Statistical Physics* 9 (3) (1973) 215–220.
- [32] A. Chorin, P. Stinis, Problem reduction, renormalization, and memory, *Communications in Applied Mathematics and Computational Science* 1 (1) (2007) 1–27.

- [33] H. Lei, N. A. Baker, X. Li, Data-driven parameterization of the generalized Langevin equation, *Proceedings of the National Academy of Sciences* 113 (50) (2016) 14183–14188.
- [34] Y. Zhu, J. M. Dominy, D. Venturi, On the estimation of the Mori-Zwanzig memory integral, *Journal of Mathematical Physics* 59 (10) (2018) 103501. doi:10.1063/1.5003467.
URL <https://aip.scitation.org/doi/10.1063/1.5003467>
- [35] M. D. Hoffman, D. M. Blei, C. Wang, J. Paisley, Stochastic variational inference, *The Journal of Machine Learning Research* 14 (1) (2013) 1303–1347.
- [36] C. Archambeau, M. Opper, Approximate inference for continuous-time Markov processes, *Bayesian Time Series Models* (2011) 125–140.
- [37] R. G. Krishnan, U. Shalit, D. Sontag, Structured inference networks for nonlinear state space models, in: *Thirty-First AAAI Conference on Artificial Intelligence*, 2017.
- [38] V. Fortuin, G. Rätsch, S. Mandt, Multivariate time series imputation with variational autoencoders, arXiv preprint arXiv:1907.04155.
- [39] J. C. Butcher, *Numerical methods for ordinary differential equations*, John Wiley & Sons, 2016.
- [40] J. Trashorras, D. Tsagkarogiannis, From Mesoscale Back to Microscale: Reconstruction Schemes for Coarse-Grained Stochastic Lattice Systems, *SIAM Journal on Numerical Analysis* 48 (5) (2010) 1647–1677. doi:10.1137/080722382.
URL <http://epubs.siam.org/doi/abs/10.1137/080722382>
- [41] M. A. Katsoulakis, J. Trashorras, Information loss in coarse-graining of stochastic particle dynamics, *Journal of statistical physics* 122 (1) (2006) 115–135.

URL <http://link.springer.com/article/10.1007/s10955-005-8063-1>

- [42] D. Kondrashov, M. D. Chekroun, M. Ghil, Data-driven non-Markovian closure models, *Physica D: Nonlinear Phenomena* 297 (2015) 33–55. doi:10.1016/j.physd.2014.12.005.

URL <http://www.sciencedirect.com/science/article/pii/S0167278914002413>

- [43] B. D. Coleman, M. E. Gurtin, Thermodynamics with Internal State Variables, *The Journal of Chemical Physics* 47 (2) (1967) 597–613. doi:10.1063/1.1711937.

URL <http://scitation.aip.org/content/aip/journal/jcp/47/2/10.1063/1.1711937>

- [44] O. Cappe, E. Moulines, T. Ryden, *Inference in Hidden Markov Models*, Springer-Verlag, 2005.

- [45] Z. Ghahramani, Unsupervised Learning, in: O. Bousquet, G. Raetsch, U. von Luxburg (Eds.), *Advanced Lectures on Machine Learning LNAI 3176*, Springer-Verlag, 2004.

- [46] D. Durstewitz, A state space approach for piecewise-linear recurrent neural networks for identifying computational dynamics from neural measurements, *PLOS Computational Biology* 13 (6) (2017) e1005542. doi:10.1371/journal.pcbi.1005542.

URL <http://journals.plos.org/ploscompbiol/article?id=10.1371/journal.pcbi.1005542>

- [47] I. Kevrekidis, C. Gear, J. Hyman, P. Kevrekidis, O. Runborg, K. Theodoropoulos, Equation-free multiscale computation: enabling microscopic simulators to perform system-level tasks, *Communications in Mathematical Sciences* 1 (4) (2003) 715–762.

- [48] L. Wiskott, T. J. Sejnowski, Slow feature analysis: Unsupervised learning of invariances, *Neural Computation* 14 (4) (2002) 715–770. doi:10.1162/089976602317318938.
- [49] C. M. Bishop, *Pattern Recognition and Machine Learning*, Springer, 2006.
- [50] D. P. Kingma, M. Welling, Auto-Encoding Variational Bayes, in: *The International Conference on Learning Representations (ICLR)*, Vol. abs/1312.6114, Banff, Alberta, Canada, 2014.
URL <http://arxiv.org/abs/1312.6114>
- [51] Y. Kim, S. Wiseman, A. C. Miller, D. Sontag, A. M. Rush, Semi-amortized variational autoencoders, arXiv preprint arXiv:1802.02550.
- [52] B. Worley, Scalable mean-field sparse Bayesian learning, *IEEE Transactions on Signal Processing* (2019) 1–1doi:10.1109/TSP.2019.2954504.
- [53] J. Li, P. G. Kevrekidis, C. W. Gear, I. G. Kevrekidis, Deciding the Nature of the Coarse Equation Through Microscopic Simulations: The Baby-Bathwater Scheme, *SIAM Rev.* 49 (3) (2007) 469–487. doi:10.1137/070692303.
URL <http://dx.doi.org/10.1137/070692303>
- [54] W. G. Noid, Perspective: Coarse-grained models for biomolecular systems, *The Journal of Chemical Physics* 139 (9). doi:http://dx.doi.org/10.1063/1.4818908.
URL <http://scitation.aip.org/content/aip/journal/jcp/139/9/10.1063/1.4818908>
- [55] D. Mackay, Probable Networks and Plausible Predictions - a Review of Practical Bayesian Methods for Supervised Neural Networks, *Network-Computation in Neural Systems* 6 (3) (1995) 469–505. doi:10.1088/0954-898X/6/3/011.

- [56] C. M. Bishop, M. E. Tipping, Variational relevance vector machines, in: Proceedings of the Sixteenth conference on Uncertainty in artificial intelligence, Morgan Kaufmann Publishers Inc., 2000, pp. 46–53.
- [57] D. P. Kingma, J. Ba, Adam: A method for stochastic optimization, arXiv preprint arXiv:1412.6980.
- [58] G.-H. Cottet, P. D. Koumoutsakos, Vortex Methods: Theory and Practice, 2nd Edition, Cambridge University Press, Cambridge ; New York, 2000.
- [59] S. Roberts, Convergence of a Random Walk Method for the Burgers Equation, *Mathematics of Computation* 52 (186) (1989) 647–673. doi: 10.2307/2008486.
URL <http://www.jstor.org/stable/2008486>
- [60] A. Chertock, D. Levy, Particle Methods for Dispersive Equations, *Journal of Computational Physics* 171 (2) (2001) 708–730. doi:10.1006/jcph.2001.6803.
URL <http://www.sciencedirect.com/science/article/pii/S0021999101968032>
- [61] M. Abadi, A. Agarwal, P. Barham, E. Brevdo, Z. Chen, C. Citro, G. S. Corrado, A. Davis, J. Dean, M. Devin, et al., Tensorflow: Large-scale machine learning on heterogeneous distributed systems, arXiv preprint arXiv:1603.04467.